2019-01-01

Ductile deformation in the Central Panamint Mountains - a multi-disciplinary approach to a multi-dimensional problem.

Tai Antonia Subia
University of Texas at El Paso, tai.subia@gmail.com

DUCTILE DEFORMATION IN THE CENTRAL PANAMINT MOUNTAINS - A MULTI-DISCIPLINARY APPROACH TO AMULTI-DIMENSIONAL PROBLEM.

TAI ANTONIA SUBIA

Master's Program in Geological Sciences

APPROVED:

Terry Pavlis, Ph.D., Chair

Benjamin Brunner, Ph.D.

Sarah Upton, Ph.D.

Stephen L. Crites, Jr., Ph.D.
Dean of the Graduate School

DEDICATION

For Waley

DUCTILE DEFORMATION IN THE CENTRAL PANAMINT MOUNTAINS - A MULTI-DISCIPLINARY APPROACH TO A MULTI-DIMENSIONAL PROBLEM.

by

TAI ANTONIA SUBIA, B.S.

THESIS

Presented to the Faculty of the Graduate School of

The University of Texas at El Paso

in Partial Fulfillment

of the Requirements

for the Degree of

MASTER OF SCIENCE

Department of Geological Sciences

THE UNIVERSITY OF TEXAS AT EL PASO

May 2019

ACKNOWLEDGEMENTS

I would like to thank the following people for their support and contributions. Ali Mahar for processing and shooting CL-imagery for SPD18, and teaching me how to interpret the resultant data. Terry Pavlis and Laura Serpa for being my academic parents. Ben Brunner for teaching me geochemistry and being a sounding board for how to simplify explanations. Gail Arnold for being my friend and mentor. My mom, Jacque, Carl, Lindsey, Malynda, Ian, Joe, Erik, Chloë, John, Claire, Amanda, Evey, Sandy, Jade, Liz, Amberlee, and Ingrid for believing in me all these years. Sal, for calling Matt and making me go climbing, and Matt and Ian for taking me climbing. We wouldn't be here if not for those actions. Y'all helped me turn my life around and I appreciate it greatly. Jade, Erik, and Georgina for being my field assistants, and Dale Zimmerman for rescuing me from a cliff in my field area. And another shout-out to Malynda for teaching me how to use the template, this process would have taken way longer without your guidance.

And finally, I have an anti-acknowledgement for the Petroleum Experts Corporation. Your company screwed over hundreds of geology students in the UT system out of greed. You should be ashamed of yourselves. You wasted our time and rendered our work unusable.

ABSTRACT

This study provides new insights into the geometry and timing of ductile, syn-metamorphic structures in the central Panamint Mountains of eastern California. The study focused on Surprise Canyon, where exposures of Meso- to Neoproterozoic miogeocline rocks, reworked crystalline basement, and syn-metamorphic granitoids record fabric overprints indicative of at least two distinct dynamo-thermal metamorphic events. Prograde metamorphism at greenschist and amphibolite metamorphic facies conditions occurred during Early Jurassic plutonism based on deformation of a dioritic pluton with a U-Pb date reported here of 175.6 ± 3.2 Ma. Mid Jurassic deformation (D1) generated the main continuous cleavage in the rocks (S1) as well as a strong lineation seen as both crystallographic alignments and object shapes. D1 is associated with numerous mesoscopic isoclinal folds with axes parallel to the sub-horizontal, NNW-ESE trending stretching lineation. Shear sense indicators are locally contradictory, presumably due to younger overprints, but with hints of a top-N sense. D1 demonstrably predates mid-Cretaceous two mica granites dated in previous studies. A second deformational event (D2) folded S1 and S1=S0 layering into upright, sub horizontal, open to tight folds that were the only structure mapped in earlier studies from the 1970's. D2 is interpreted as a Laramide age event with west-vergent fold systems.

Because of the complexity of the deformation, this study employed a chemostratigraphic analysis of marbles to test assumed correlations of these units with known stratigraphy that show distinctive light stable isotope signatures. This chemostratigraphy methods used in this study generally confirmed previous correlations, however it should be noted the method works best in sections where rock units maintain their primary stratigraphy. This study also hoped to test the hypothesis that the Harrisburg detachment mapped in the northern Panamint Mountains was

present in Surprise Canyon. In Surprise Canyon, however, rocks at the assumed structural level of this detachment are disrupted along a high-angle, brittle fault mapped in previous studies as the Woodpecker fault. Thus, future work needs to address this question along strike where this brittle fault does not disrupt the ductile structure.

TABLE OF CONTENTS

LIST OF TABLES

LIST OF FIGURES

LIST OF PLATES

INTRODUCTION

Southeastern California is well known for its long and intricate geologic history recorded in the Death Valley region. The *ca.* 1.8 billion-year-old geologic record encapsulates a history that began during the Mesoproterozoic, documenting depositional environments and multiple deformation events that occurred during the assemblage of what is now the southwestern Cordillera (Figure 1). This geologic history has contributed unique strain signatures to the rocks exposed to the stresses imposed by multiple orogenies. The structural complexities found throughout the region range from the well-studied extensional to older contractional structures that include ductile deformation in the Panamint, Black, and Funeral Mountains (Wright & Troxel, 1967). The Wildrose and Surprise Canyons of the central Panamint Mountains display examples of these structural complexities in three-dimensional exposures.

To date most of the work in the area has approached the problem of accounting for how much Cenozoic translation has occurred in the Death Valley region as a two- or three-dimensional (two spatial dimensions, and time) analysis of a four-dimensional (three spatial dimensions, and time) problem (Serpa & Pavlis, 1996). This has led to difficulties in creating robust restorations of the Death Valley region. In Wildrose Canyon, Hodges et al. (1990) used a 2D cross-section model to restore a cover of weakly metamorphosed to unmetamorphosed Neoproterozoic to Paleozoic rocks along the Emigrant detachment to its pre-Miocene position. In this restoration, a second detachment was inferred beneath the Emigrant pass system, the Harrisburg fault. These structures were then restored above the Black Mountains along the Amargosa fault system, and the authors of the study concluded the "resultant geometry is characteristic of Cordilleran metamorphic core complexes" (Hodges et al., 1990). Similarly, Norton (2011) used the Harrisburg detachment to

infer a domal fault system that is connected to the western boundary fault of the Panamint Mountains, invoking an even larger scale core-complex type system.

In contrast, Labotka and Albee (1990) avoided the term ‘core complex’ for the Panamint Mountains and emphasized the tilted extensional block style of the range. Curiously, in the core complex models of the Panamint Mountains that emphasize the Harrisburg detachment (Hodges, McKenna, & Harding, 1990; McKenna & Hodges, 1990; Norton, 2011) the descriptions of the “Harrisburg detachment” are cursory at best. Inspection of geologic maps of these areas (Albee, Labotka, Lanphere, & McDowell, 1981; Harding, 1987) do not reveal an obvious structure corresponding to the Harrisburg fault. For example, in the geologic map of Wildrose Canyon (Harding, 1987) the Harrisburg fault was described by Hodges et al. (1990) as a structure separating the Noonday Dolomite from the Johnnie Formation and cross cut by the Little Chief Stock. Yet the Johnnie Formation is in normal stratigraphic succession with Noonday Formation in Wildrose Canyon, suggesting that a fault or shear zone at this level, if present at all, would have minimal stratigraphic throw. Although complex geometric scenarios are possible, this association suggests that core-complex type scenarios that use the Harrisburg detachment as a major structure are unlikely.

Original mapping of the Panamint Mountains (Albee et al., 1981) suggested a relatively simple antiformal structure with a NS trending fold axis. However, recent work indicates this interpretation is a gross oversimplification (Brush et al., 2015; Cobb, 2015; Pavlis et al., 2016). Hints that the original work oversimplified the structure are also present in Labotka’s work on the metamorphic petrology which showed that the rocks reach upper amphibolite facies in the western Panamint Mountains (T. C. Labotka, 1981). Such simple structure would be unlikely in a scenario

of 500º C to 600º C temperatures, pressure conditions varying from two to three kilobars, and considering the stresses related to the emplacement.

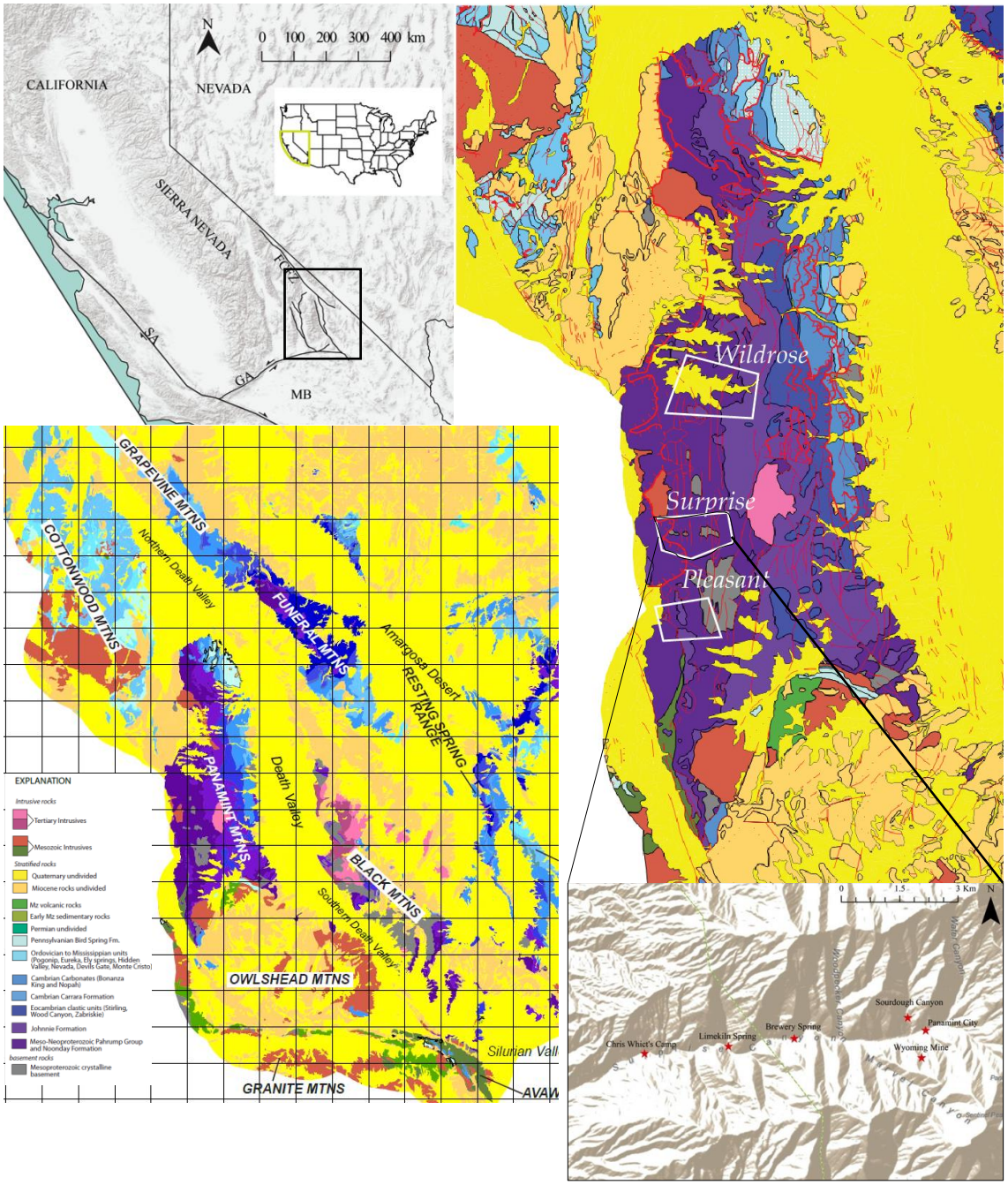

Figure 1. Geography of Death Valley region and the Central Panamint Mountains Regional geologic maps by Pavlis et al., 2014 after Albee et al, 1981, and Workman et al., 2002.

of the Sierra Nevada batholith ~50 kilometers to the west, as well as the west to east vergence of the Kula and Farallon plates during subduction (Dickinson, 2004). Hodges et al. (1987)

demonstrated that rocks in the northern Panamint Mountains, which are of lower metamorphic grade than the west-central part of the range, underwent three distinct folding events, with two early events transposing bedding by isoclinal folding, Figure 3A and 3B. Andrew (2002) mapped D1 structures on the western flank the southern Panamint Mountains, and in Goler Canyon an outcrop of horneblende diorite exhibits a shear zone that displays S-C fabrics and tops to the east shearing of east vergent folds (Figure 3G). U-Pb analysis was conducted on a sample of this diorite using thermal ionization mass spectrometry and produced a date of 175.6 ± 1.2 Ma (Andrew, 2002). Based on careful mapping of amphibolite facies metamorphic structures in Surprise and Pleasant Canyon Cobb (2015) and Brush (2015) confirmed that these complex structures of the northern Panamint Mountains also occur in the central Panamint Mountains.

Cobb (2015) showed juxtapositions putting marbles interpreted as Beck Spring above lower Kingston Peak schists. This is inconsistent with the known stratigraphy of the Proterozoic Pahrump Group. Prior interpretations have attributed these juxtapositions to syntectonic deposition during Neo-Proterozoic rifting (Labotka et al., 1980). While some of the juxtapositions may be attributed to syndepositional unconformities (Labotka et al., 1980) that developed during the rifting of Rodinia (Smith et al., 2016), it is difficult to reconcile the distribution of rock units in parts of the western Panamint Mountains as a primary stratigraphic relationship. For example, in central Surprise Canyon to the east of Limekiln Spring (FIGURE 1) a white marble found below the glacial diamictite of the Kingston Peak Formation is at least 260m thick. Yet, to the west, below Limekiln Spring, marbles that presumably correlate based on position and continuity on imagery to the north and south are less than 20m thick and pinch out laterally (Cobb 2015). This variation could reflect erosional thinning along an unconformity beneath the diamictite or Precambrian faulting, but given the structural complexity it is more likely caused by variations in

finite strain. Aside from equivocal correlations of rock units, the stratigraphic younging is unknown in most of these units given the clear evidence for isoclinal folding. Because the glacial diamictites in this region are both overlain and underlain by carbonate rocks (Smith 2016), it is possible the marbles have been miscorrelated; e.g. the section may be overturned.

Fortunately, extensive work has been done on the stratigraphy of this region. Of particular significance is a large chemostratigraphic record of the major carbonate units within the Pahrump Group and the overlying cap carbonates that were deposited in the Pahrump basin during the Meso- and Neoproterozoic eras (Prave, 1999; Corsetti & Kaufman, 2003, 2005). The studies of Prave (1999), Corsetti and Kauffman (2003, 2005), Petterson, et al. (2011), MacDonald, et al. (2013), and Smith, et al. (2016) demonstrate that each of the carbonate units within the Pahrump Group have distinctive carbon and oxygen isotope signatures. The studies of Petterson (2011) and Smith (2016) have shown that there is no significant deviation in the carbonate-carbon isotope composition caused by metamorphism. This finding suggests that even reconnaissance sampling and carbon isotope analyses of marbles can be used to readily distinguish the different carbonate units.

This study focused on Surprise Canyon, where the exposed Meso- to Neoproterozoic miogeocline rocks have undergone two known metamorphic events (Figure 4). Prograde metamorphism due to burial depth of ~10 kilometers, with greenschist and amphibolite metamorphic facies conditions occurred during Mesozoic plutonism and increases in grade from east to west in the Panamint Mountains (Lanphere et al., 1964; Evernden & Kistler, 1970; Labotka et al., 1980; Andrew, 2002). Younger, retrograde metamorphism occurred due to emplacement of the Skidoo-Hall Canyon pluton in Wildrose, Hall, and Surprise Canyons in the Late Cretaceous (Labotka et al., 1980; Labotka, 1981; Cobb, 2015). Recent mapping by Cobb (2015), Brush (2015)

and Pavlis (unpublished data) have shown that the structure of the western Panamint Mountains is much more complex than indicated in earlier mapping by Albee et al. (1981).

The purpose of this study was:1) to resolve ambiguities in correlations between rock units through the central Panamint metamorphic assemblage, 2) to give further time constraints of deformation events in the area, and 3) evaluate evidence for the existence of the Harrisburg fault in Surprise Canyon. This was done by combining detailed 3D mapping techniques with chemostratigraphic reconnaissance, and U-Pb geochronology. To accomplish this, the rocks in central Surprise Canyon were mapped from the Limekiln Spring Fault past Panamint City in the eastern end of the canyon, where the low-grade metamorphic to metasomatized rocks clearly retain their primary stratigraphy (Figure 2 and Plate I), up to Water Canyon where the middle and upper Pahrump Group strata come into contact with the Little Chief Stock. During mapping, samples were collected from the marbles exposed within Surprise Canyon. These marble samples were then analyzed for their carbon isotope composition ($\delta^{13}C$) for comparison with the known $\delta^{13}C$ values of the Beck Spring Dolomite and the Noonday Formations. Samples of a boudinaged granodiorite sill were also taken for geochronologic analysis. These data were combined with detailed geologic mapping and construction of a set of cross-sections to develop a 3D geologic model of central Surprise Canyon to better understand the cross-cutting relationships of deformation events. Collectively, the mapping, isotopic analyses, and U-Pb geochronology data have aided in resolving the issues of correlating the metamorphosed Neoproterozoic rock units. These new correlations improve the understanding of the structure and tectonic history of the central Panamint metamorphic assemblage.

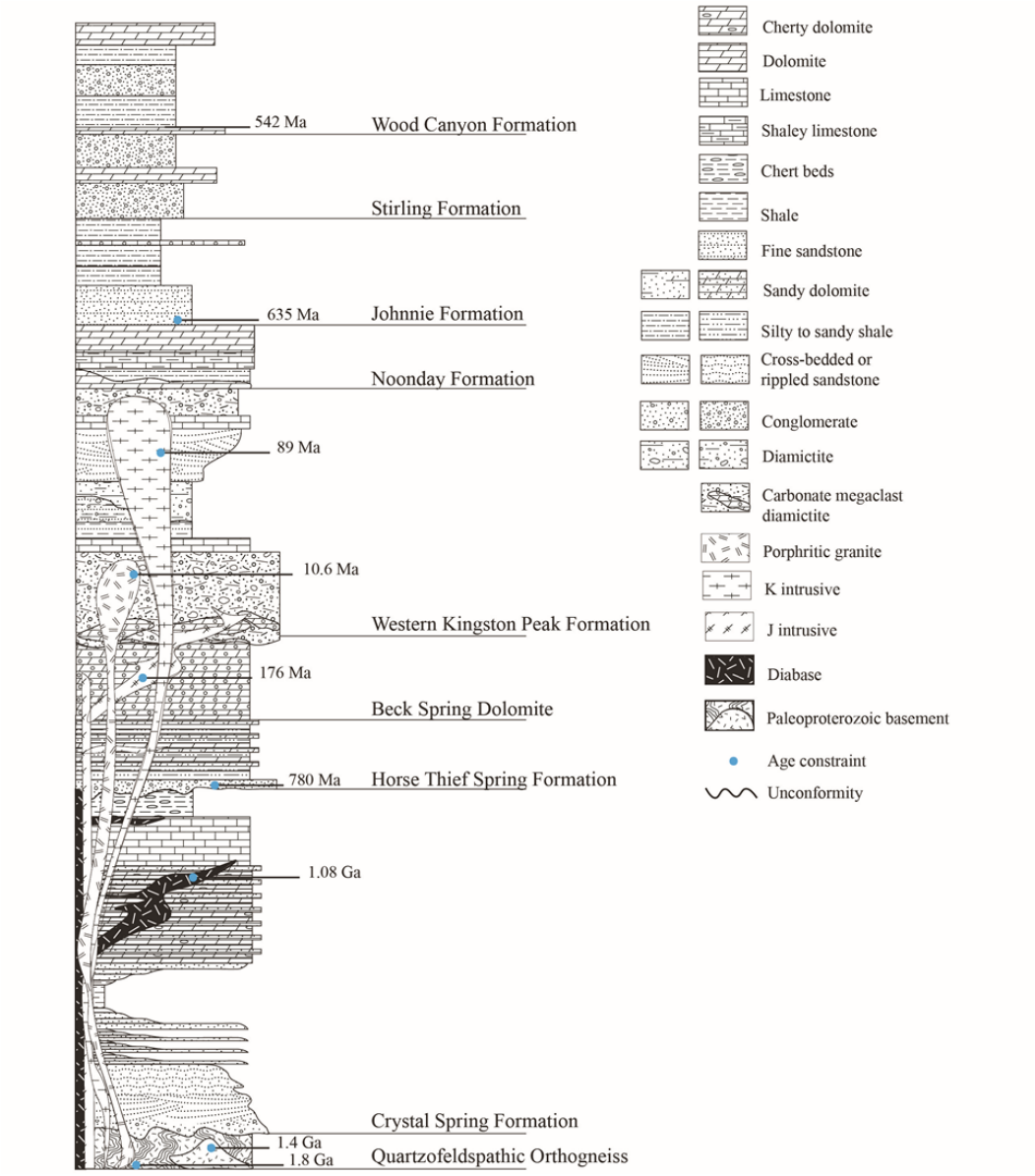

Figure 2. Stratigraphy of Surprise Canyon in the Panamint Mountains

Compiled from Wright & Troxel, 1968; Stewart, 1970; McDowell, 1973; Roberts, 1976, 1982; Maud, 1979, 1983; Labotka et al., 1980; Miller, 1985; Heaman & Grotzinger, 1992; Prave, 1999; Corsetti and Kauffman, 2003; Calzia and Ramo, 2005; Mrofka & Kennedy, 2011; Petterson et al., 2011; Macdonald et al., 2013; Mahon et al., 2014; Cobb, 2015; Smith et al., 2015

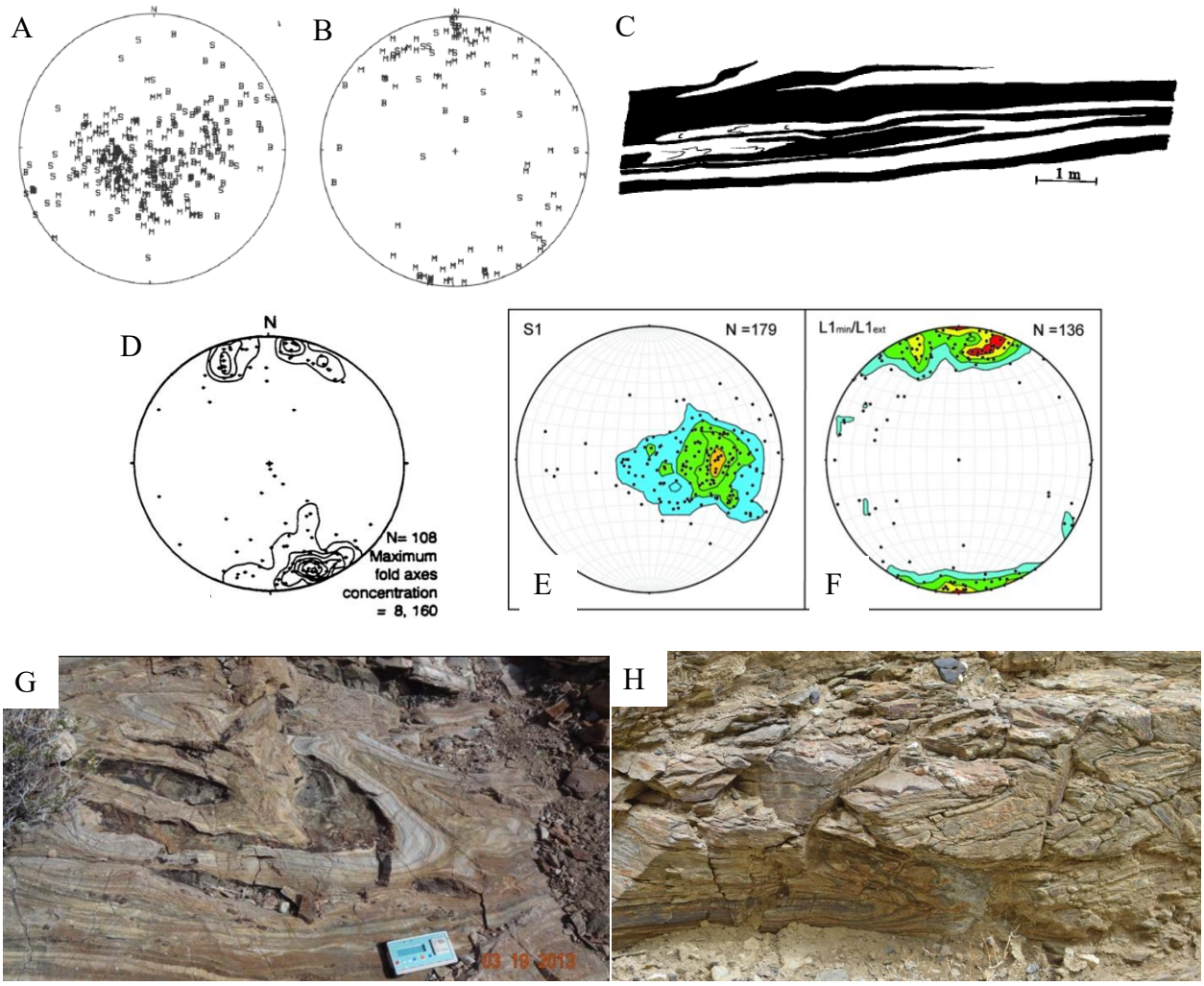

Figure 3. Fabrics of the Panamint Mountains

Stereonets depict orientation data related to D_1 recorded in both the low and high-grade metamorphic rocks of the northern, central, and southern Panamint Mountains, respectively. A) π diagram of the poles to $S_{1\text{-}2}$ schistosity and $F_{1\text{-}2}$ axial planes, B) plot of measured $F_{1\text{-}2}$ axes, C) Fold morphology sketch is a representation of the principle section of the $F_{1\text{-}2}$ structure found in and around Tucki Mountain; insets A, B, and C are modified from Hodges et al., (1987). D) F1 axes from the southern Panamint Mountains, modified from Andrew (2002). E) S1 from Pleasant Canyon, and F) Mineral and stretching lineations from Pleasant Canyon are modified from Brush 2015. G) Photograph of isoclinal folds in the Noonday Formation located in Pleasant Canyon, by Brush (2015). H) Photograph of D_1 structures found in lower Surprise Canyon, by Pavlis et al., (2016).

REGIONAL GEOLOGY

The Death Valley region represents a unique window into the geologic history of North America. Powell's (1876) Great Unconformity, originally noted in the Grand Canyon, has

obliterated up to 1.2 billion years of the geologic record from the American Southwest, with southeast California being an exception. Here the Meso- to Neoproterozoic rocks of the Pahrump Group were preserved by miogeoclinal deposition along a longstanding passive margin that lasted well into the Later Paleozoic, until the Late Devonian initiation of the Cordilleran orogenesis (Busby-Spera et al., 1990; Stevens et al., 1997).

Deposition of the Pahrump Group occurred on the southwest margin of Laurentia during the assemblage and rifting of Rodinia (Macdonald et al., 2013; Mahon, Dehler, Link, Karlstrom, & Gehrels, 2014; Smith et al., 2016). The succession overlies the ca. 1.78 – 1.66 Ga granitic gneiss of the Mojave Crustal Complex which extends southeast of Death Valley (Wasserberg et al., 1959; Barth et al., 1995; Strickland et al., 2013), and the ca. 1.43-1.4 Ga porphyritic quartz monzonite intrusion found in the Panamint Mountains (Wasserberg et al., 1959; Lanphere et al., 1964; Labotka et al., 1980). Cobb (2015) used laser-ablation multi-collector inductively coupled plasma source mass spectrometry analysis of zircons to obtain U-Pb geochronology and refine the dates of the quartzofeldspathic gneiss described by Labotka et al. (1980) and mapped by Albee (1981). Outcrops of this gneiss can be seen in Pleasant and Surprise Canyons. The analyses indicate Paleoproterozoic zircon dates within the range of 1789.9 ± 4.0 Ma and 1809.8 ± 4.7 Ma, however, complex internal structures are observed in the zircons and some dates correspond to Mesozoic ages indicating an overprinting event that took place (Cobb, 2015).

Beginning with the Crystal Springs Formation, the Pahrump Group is comprised of sediments whose deposition was initiated in the upper Mesoproterozoic during the assemblage of Rodinia on a S-SW facing open margin (Smith et al., 2016). The informal members of the formation in ascending order are the basal arkosic sandstone, feldspathic sandstone, mudstone, dolomite, algal dolomite-siltstone, and chert members (Wright & Troxel, 1968; Roberts, 1976,

1982; Mahon et al., 2014); all members are intruded by diabase sills. Wright and Troxel (1968), and Hammond (1983, 1986) proposed that these sills intruded while the Crystal Springs sediments were wet and unconsolidated, giving a relative date of deposition (Wright & Troxel, 1968; J. L. G. Hammond, 1983; J. G. Hammond, 1986). Using thermal ionization mass spectrometry Heaman and Grotzinger (1992) produced U-Pb, ages of ca. 1.08 billion years from samples taken from two sills; one in the Black mountains, the other in the Kingston Range (Heaman & Grotzinger, 1992).

An unconformity originally identified by Maud (1979, 1983) in the Saddle Peak Hills that was thought to be an internal unconformity within the Crystal Springs Formation between the middle and upper units was later identified to be of regional scale (Mbuyi & Prave, 1993). The upper unit is ca. 105 to 460 meters thick and is comprised of six sequences of dominantly siliciclastic rocks that are each overlain by a bed of dolomite, and a final upward fining sequence that is in gradational contact with the Beck Springs Dolomite above (Maud, 1979, 1983; Smith et al., 2016). The siliciclastic strata include green and purple argillite, immature quartz arenite, locally arkosic and poorly sorted quartzitic conglomerate containing chert nodules from the chert bed of the Crystal Springs (Maud, 1979, 1983; Smith et al., 2016). Siliciclastic beds dominate the southwest sections with the thickest of these sections located in Beck Canyon in the Kingston Range, and carbonate beds dominate in the northeastern sections (Smith et al., 2016). This evidence, along with paleoflow measurements suggests a southern sediment source with a NW-SE trending shoreline and basin depth increasing to the northeast (Maud, 1979, 1983; Smith et al., 2016). Mahon (2014) tested detrital zircons taken from the base of the unit overlying the disconformity resulting in a maximum depositional age of ca. 787 Ma, showing a ca. 300-million-year unconformity between the lower and middle Crystal Springs members and the base of the overlying member. This unconformity represents a period of tectonic inactivity and correlates

regionally to other Proterozoic successions. The unit, long considered the upper member of the Crystal Springs Formation, has been renamed the Horse Thief Springs Formation (Mahon et al., 2014).

Deposition of the Beck Spring Dolomite occurred from ca. 780 Ma to ca. 717 Ma, prior to the Sturtian glaciation event of the Cryogenian, with thicknesses varying from 110 to 320 meters (Smith et al., 2016). To the east and south of Death Valley the formation contains preserved eukaryotic microfossil assemblages, and diverse microbialites interbedded with siliciclastic strata in the southern exposures (Smith et al., 2016). To the northwest in the Panamint Mountains, the formation has been recrystallized and thoroughly foliated. There are large carbon isotope anomalies recorded directly below the Kingston Peak Formation (Macdonald et al., 2013; Smith et al., 2016). Smith's (2016) detrital zircon analyses indicate the provenance to be from the Mojave block. Coupled with the character of the lateral sedimentary facies changes from siliciclastic beds in the southwest to carbonate beds in the northeast, intra-formational thickness variations, and the presence of syn-sedimentary faults (Macdonald et al., 2013; Smith et al., 2016) suggest that the Beck Spring Dolomite and the basal Kingston Peak Unit (referred to as KP1) deposition fringed a coeval paleo-high to the south-southwest in a tectonically active basin undergoing subsidence due to dextral shearing related to far field stresses from large igneous province emplacements (Smith et al., 2016). The Beck Spring Dolomite shares a gradational contact, and genetic relationship with the overlying KP1 representing a major transgression and influx of fine siliciclastic sediments in the basin (Miller, 1985; Wright, et al., 1992; Prave, 1994; Mrofka, 2010; Macdonald et al., 2013; Smith et al., 2016).

The final member of the Pahrump Group is the Kingston Peak Formation. There are two distinct glaciogenic facies, the eastern and western facies packages. They are referred to as the

Eastern Kingston Peak Formation (EKPF) located east of Death Valley, whereas the Western Kingston Peak Formation (WKPF) is located in the Panamint Range (Miller, 1985; Mrofka & Kennedy, 2011; Petterson et al., 2011). The EKPF can be further divided into the northern facies (Troxel, 1966) and the southern facies (Troxel, 1967). The facies are divided by the siliciclastic compositions of the diamictites and their position within the basin. The deposition occurred in an intra-cratonic rift basin deepening to the north; this basin experienced two discrete rifting episodes (Wright et al., 1976; Labotka et al., 1980; Miller, 1985; Prave, 1999; Petterson et al., 2011).

The KP1 is the basal member of the EKPF northern facies. The unit is 1 to 180 meters thick, contains siltstones and fine-grained arkosic sandstones without glaciogenic features (Miller, 1985; Wright et al., 1992; Mrofka, 2010; Macdonald et al., 2013; Smith et al., 2016). The base of the KP1 includes what was thought to be karst breccias at the top of Beck Spring Dolomite, but is now thought to be composed of massive debris flows (Smith et al., 2016). Faulting, folds, turbidite flows, and soft sediment deformation within the KP1 created high angle unconformities that were sealed by the Virgin Spring Limestone. In the Alexander Hills and the Kingston range, an erosional surface truncated the Virgin Spring Limestone down into the KP1; this surface separates the KP1 from the KP2 (Mrofka & Kennedy, 2011; Macdonald et al., 2013).

The Virgin Spring Limestone (VSL), named for the Virgin Spring Wash of the southern Black Mountains where the 10-meter type section is exposed in outcrop, is 4 to 17 meters thick, with the thickest exposure of 17 meters in the Ibex Hills. The unit shows erosional truncation increasing to the south and east in the Saratoga and Saddle Peak Hills where the unit is ~4 meters thick (Mrofka & Kennedy, 2011; Macdonald et al., 2013). The Virgin Spring Limestone is comprised of 1 to 10 centimeter black laminated limestone interbedded with millimeter scale fine sandstone laminae, and contains Pre-Sturtian vase-shaped microfossils (Tucker, 1986; Macdonald

et al., 2013). The erosional truncation at the top of the VSL and into the KP1 in the Alexander Hills and Kingston Range is a regional unconformity separating the KP1 and VSL package from the glacial deposits of the KP2 through KP4 (Mrofka, 2010; Smith et al., 2016). These glacial deposits mark the beginning of the Sturtian glaciation event ca. 717 Ma and record events related to the rifting of the western margin of Laurentia (Mrofka, 2010; Mrofka & Kennedy, 2011; Petterson et al., 2011; Smith et al., 2016).

The KP2 Member is 10 to 250 meters thick and contains cobble and boulder sized clasts of the underlying units, with a few clasts showing either striations or facets. The basal KP2 contains clasts of the VSL and a carbonate rich matrix that coarsens upward into in a coarse, angular sand matrix containing illite, and/or chlorite (Mrofka, 2010; Mrofka & Kennedy, 2011). The KP3 Member is a 15–2000 m thick wedge. It consists of interbedded siltstone and sandstone which is overlain by a 2 to 3 meter thick oncolitic dolomite bed that coarsens upward into interbedded sandstones and diamictite with striated clasts, normally graded conglomerate beds, kilometer-scale blocks of the Beck Spring Dolomite called olistoliths which formed due to extensional tectonics associated with the rifting of the supercontinent Rodinia, and channel filling sedimentary breccias (Mrofka, 2010; Mrofka & Kennedy, 2011; Smith et al., 2016). The KP4 Member gradationally overlies the KP3 Member and comprises 200–1300 m of conglomerate, sedimentary breccia and mega-breccia derived from the Beck Spring Dolomite due to syndepositional faulting. Laterally to the north, these sedimentary breccias and conglomerates are interbedded with normally graded and massive sandstones (D. Mrofka & Kennedy, 2011).

The southern facies of the EKPF is dominated by clasts of basement granite and gneiss, and is only found in the southern Saddle Peak Hills, and the Silurian hills (Troxel, 1967; Mrofka & Kennedy, 2011). The basal unit of the southern facies is Kupfer's (1960) unnamed limestone

and has been correlated to the Thorndike Limestone sub-member of the South Park Member of the WKPF by Prave (1999), using carbon isotope compositions and quartzite conglomerates found in outcrop below both limestone beds (Kupfer, 1960; Prave, 1999; Mrofka & Kennedy, 2011).

The WKPF located in the Panamint Range is comprised of interbedded diamictites, immature sandstones, and argillites, with the diamictites ranging from poorly bedded to massive deposits (Miller, 1983; Petterson et al., 2011). In the central Panamint mountains, the western facies package has been exposed to greenschist and amphibolite metamorphic facies during Middle Mesozoic emplacement of plutons in the Inyo and White Mountains, with the metamorphic grade increasing east to west (Evernden & Kistler, 1970; Labotka et al., 1980; Petterson et al., 2011). The formal member names from base upward are the Limekiln Spring Member, Surprise Diamictite, Sourdough Limestone, South Park Member, and the Wildrose Diamictite.

The Limekiln Spring member is a structurally complex unit 0 m to 1000 m thick with lateral and vertical variability with beds thinning to the east. This variability of thickness and lateral continuity has been attributed to the paleotopography of the underlying basement (Labotka, 1978; Labotka et al., 1980; Miller, 1985). In the southern area of the Panamint Range near Goler Wash, the Limekiln Spring member consist of interbedded diamictite, sandstone, and siltstone beds (Miller et al., 1988). In the Telescope Peak area, the Limekiln Spring member has been subjected to greenschist and amphibolite facies and is comprised of immature sandstones, pelitic schists, amphibolite, minor dolomitic marble, and intermittent lenses of metaconglomerates and breccias (Labotka et al., 1980; Miller et al., 1988; Pettersonet al., 2011).

The Limekiln Spring member is likely coeval with the KP1 of the eastern sedimentary facies and is visible in outcrop in the southern Panamint Range and North of Telescope Peak (Mrofka & Kennedy, 2011; Petterson et al., 2011; Smith et al., 2016). The Surprise Diamictite is

probably correlative to the KP3 of the EKPF. This member contains cubic kilometer scale olistoliths of the Beck Spring dolomite as well as older units, odd mafic bodies, and buried normal faults; this evidence supports syn-sedimentary extensional tectonism (J. M. G. Miller, 1983; Julia M. G. Miller, 1985; A. R. Prave, 1999; D. D. Mrofka, 2010; D. Mrofka & Kennedy, 2011). Olistoliths are visible in Happy and Surprise Canyons (Smith et al., 2016).

The Surprise Diamictite is poorly bedded to massive in the southern part of the Panamint Range, with the facies fining basin ward, to the north. The member contains mafic dikes and pillow basalts ca. 10 to 35 meters thick (Hammond, 1983), with the thickest exposure in Goler Wash (Miller, 1983; Miller, 1985). The Surprise diamictite is ~1300 meters thick west of Telescope Peak, but given the structural complexity, the unit there is probably structurally thickened, but difficult to evaluate because of absence of primary bedding and dominance of secondary fabric development. The clast composition is sub rounded to rounded quartzite clasts, and sub angular carbonate clasts all ranging in size from pebbles to boulders. The clasts are supported in an argillaceous, sandy matrix, with minor dark grey argillite beds local to the range (Miller, 1985; Petterson et al., 2011). North of Telescope Peak the diamictite becomes uncommon and the lithology becomes dark grey to black argillites and fine sandstones interbedded with argillaceous limestone (Labotka et al., 1980). The transition of the facies from diamictites in the south to fine siliciclastics in the north is structurally complex, with some uncertainty about the facies being coeval (Labotka, 1978; Labotka et al., 1980).

The Sourdough Limestone is interpreted as a cap carbonate overlying the lower glacial deposits; the limestone is graphite rich, and shows intense internal deformation and recrystallization in areas of high metamorphic grade (Miller, 1985; Petterson et al., 2011). The Sourdough is overlain by the South Park member which contains interbedded sandstones and

pelites, thin diamictite layers, a quartzite conglomerate and the Thorndike Limestone, another cap carbonate. These limestone sub-members represent two warming periods within the Cryogenian (Corsetti & Kaufman, 2003, 2005; Petterson, Prave, Wernicke, & Fallick, 2011; A. R. Prave, 1999; Anthony R. Prave, 2000). The final member of the WKPF is the Wildrose Diamictite, a massive matrix supported diamictite with abundant gneiss clasts (Petterson et al., 2011).

Above the KPF is the Noonday formation. The Noonday is interpreted as a cap carbonate that marks the end of Marinoan glaciation at the end of the Cryogenian period, and the start of the Ediacaran period (Petterson et al., 2011). Adding to the multiple unconformities found throughout the Pahrump Group succession, the base of the Noonday Formation regionally sits on all of the underlying units, including basement (Wright, 1954; Prave, 1999; Macdonald et al., 2013). The formation is comprised of three formal members, the basal Sentinel Peak, the Radcliff, and the Mahogany Flats members (Petterson et al., 2011). The Sentinel Peak member is laminated to massive dolomite with microbial tubestone mounds interbedded with limestone, siltstone, sandstone, and carbonate breccias. The Radcliff Member contains siltstones, silty dolostone, arkosic sandstones and shales, and intraformational breccias. The Mahogany flats member is dolomitic sandstones and grey stromatolitic dolostone (Petterson et al., 2011). The tubestone algal mounds of the Sentinel Peak member terminate to the south of Manly peak and the Saddle Peak Hills (Hazzard, 1937; Johnson, 1957; Wright & Troxel, 1967). After the rifting of the western margin of Laurentia, passive margin deposition continued with the Johnnie Formation, Stirling Quartzite, Wood Canyon Formation, up through the Permian. These units are outside the study area and can be found in outcrop in the east, on the Death Valley side of the Panamint Mountains (Labotka et al., 1980; Stevens et al., 1997).

TECTONIC AND CLIMATE EVENTS – CONTROLS ON THE ROCK RECORD

The Crystal Springs Formation represents deposition during the assemblage of Rodinia, and the 300-million-year unconformity between the Crystal Springs formation and the Horse Thief Springs Formation represents a long period of tectonic quiescence (Mahon et al., 2014). The Horse Thief Springs Formation, the Beck Spring Dolomite, Kingston Peak Formation, and the overlying Noonday Dolomite and Johnnie Formation represent deposition that occurred within basins created by tectonothermal events related to far field stresses from large igneous provinces (Smith et al., 2016), and the initiation of the rifting of Rodinia in the mid Cryogenian, through the final separation of Laurentia along the southern and western margins in the mid Ediacaran (Mahon et al., 2014). It was during the late Cryogenian period where glaciation was extensive, nearly reaching the equator (Macdonald et al., 2010; Rose & Maloof, 2010). Deposition of cap carbonates during warming periods caused by massive CO_2 emissions are recorded by variations of light stable isotope compositions of carbon and oxygen in the cap carbonates of the Kingston Peak and the basal Noonday Formation (Prave, 1999; Mrofka, 2010; Petterson et al., 2011). These variations can be correlated to other formations deposited during the near global scale glaciation events during the Cryogenian period (Hurtgen et al., 2004).

The Crystal Spring Formation can be correlated to the Unkar Group of the Grand Canyon indicating a regional tectonostratigraphic unit that formed in active rift basins responding to the Grenville orogeny during the assembly of Rodinia (Timmons et al., 2001; Timmons et al., 2005; Smith et al., 2016). The Horse Thief Springs Formation, Beck Spring Dolomite, and the KP1 of the Kingston Peak Formation (Prave, 1999; Macdonald et al., 2013) correlate with the Chuar Group, also of the Grand Canyon, defining a regional tectonostratigraphic unit deposited in transtensional intracratonic basins that formed a broad interior seaway during the primary stages

of the breakup of Rodinia (Timmons et al., 2001; Dehler et al., 2001, 2005; Macdonald et al., 2013; Mahon et al., 2014; Smith et al., 2016). KP2 through KP5 and the WKPF correlations record rifting, synglacial deposition, and two discrete warming events within the Cryogenian period (Miller, 1985; Prave, 1999; Mrofka, 2010; Mrofka & Kennedy, 2011; Petterson et al., 2011).

Following the breakup of Rodinia, passive margin deposition developed in the latest Ediacaran to early Cambrian time and continued through the late Devonian. Subsidence in the east central California region outpaced sedimentation as evidenced by retrograding development of carbonate platforms to the southeast (Stewart, 1970; Armin & Mayer, 1983; Stevens, 1986; Stevens et al., 1997; Fedo & Cooper, 2001; Smith et al., 2016). Miogeoclinal sedimentation and subsidence of the passive margin of SW Laurentia ended in the Late Devonian with the onset of widespread contractional tectonism related to the Antler Orogeny, and continental scale sinistral shearing and fast basin subsidence occurring until the Early Triassic (Stevens et al., 1997). The front of the orogenic belt is located in west central Nevada in the area north of Miller Mountain, northeast of the White Mountains (Stewart & Poole, 1974; Stevens et al., 1997). This long period of contractional tectonism was followed by a period of subsidence and passive sedimentation for the remainder of the Early Triassic period. There is no concrete evidence of syndepositional tectonism or magmatism in east central California during this time (Stevens et al., 1997).

Tectonic quiescence ended in the east California region during the Middle Triassic when stresses related to the Sonoma Orogeny began to deform the land. Pendants of Cambrian to Devonian meta-sediments juxtaposed with upper Paleozoic meta-sediments are preserved in the Sierra Nevada directly west of the White and Inyo Mountains. These pendants display deformation related to the Sonoma orogeny and possibly the Antler orogeny, and are cross cut by faults. These

faults were truncated by the intrusion of plutons ca. 222 ±5 Ma and 225 ±16 Ma (Speed & Lintz Jr, 1984; Schweickert & Lahren, 1987; Greene, et al., 1997).

The east dipping subduction of the Farallon plate beneath the North American plate caused east central California, and hence what would become the Panamint Mountains and surrounding areas, to undergo several cycles of deformation during the Mesozoic era. These effects of the compressional and transpressional stresses were compounded by the local stresses associated with the prolific magmatism that produced the Sierra Nevada batholith complex during the Mid-Jurassic. Geographically the region sat on the flank of the growing magmatic arc (Burchfiel et al., 1992; Stevens et al., 1997). Plutons radiometrically dated in the El Paso Mountains, Owens Valley, and Mono Lake Basin show the easternmost extent of plutonism that initiated during the Late Triassic; however, it is possible that magmatism was not sparse, but the evidence may have been radiometrically reset by subsequent and more voluminous episodes (Armstrong & Suppe, 1973; Stevens et al., 1997). There is little regional evidence for Early Jurassic plutonism, however Armstrong and Suppe (1973) extracted a K-Ar date of 194 Ma from hornblende of a granodiorite collected from the San Bernadino Mountains. Other dates obtained in the region for this time frame are older than 200 Ma, or younger than 185 Ma (Miller, 1978; Busby-Spera et al., 1990; Andrew, 2002; Rämö et al., 2002) .

Plutonism had peaked in terms of volume and extent by the Mid-Jurassic. It was during this time that much of the Sierra Nevada batholith was emplaced. The range is a composite of granitoid intrusions generated during this Mid-Jurassic plutonism episode, as were several other large batholiths in east central California, including the Inyo Batholith (Lanphere et al., 1964; Evernden & Kistler, 1970; Stevens et al., 1997).

Dunne et al., (1998) found evidence that the volcanic complexes developed coeval to the plutonism in the southern White Mountains, and in Butte Valley of the southern Panamint Mountains to have been associated with large volcanic centers that formed in periods of high magma flux during this time. Thick sequences of volcanic epiclastic sediments in large subaerial fluvial systems with northeast draining paleoslopes formed on these moderate to high relief volcanic complexes (Stevens et al., 1997; Dunne et al., 1998). Emplacement of the Manly Peak Pluton in the southern Panamint Range occurred ca. 149 Ma (Rämö et al., 2002). In the Late Jurassic, dike swarms became the primary magmatic activity. The Independence Dike Swarm, is a 500-kilometer long, northwest trending mafic dike system in east central California, with zircon U-Pb dates ca. 148 million years (Chen & Moore, 1979; Stevens et al., 1997).

The stratigraphy of east central California was subject to episodes of regional-dynamothermal metamorphism due to the prevalent magmatism in the arc and arc-flank provinces throughout the Mesozoic. Deformation during arc emplacement produced the East Sierra Thrust System (ESTS), and northwest trending fold and thrust belt comprised of northeast verging thrusts, reverse faults, folds, and rare conjugate strike slip faults and shear zones located along the eastern margin of the Sierra Nevada (Stevens et al., 1997; Dunne et al., 1998). The dips of faults associated with the ESTS range from ca. 30 to 90º SW with an average dip of ca. 55º SW. These thrusts are ductile with zones of exotic lenses and host well developed examples of stretching lineations oriented to known or inferred slip direction of the faults. The ESTS type area extends from the southern Owens Valley to the Garlock Fault with a maximum width of 20 kilometers from the eastern margin of the magmatic arc (Stevens et al., 1997).

Contractional deformation related to the ESTS occurred from the Late Triassic through the Late Cretaceous. Late Triassic deformation is recorded in the Saddlebag Lake Pendant, in the Inyo

Mountains and Darwin Hills (Stevens et al., 1997). Latest Jurassic deformation of volcanic complexes in the Inyo Mountains and Slate Range has been truncated by the Independence Dike Swarm emplacement ca. 148 million years ago (Chen & Moore, 1979; Stevens et al., 1997). Mid to Late Cretaceous ESTS deformation structures are found in the northern Inyo Mountains, White Mountains, Benton Range, and Saddlebag Lake pendant. Based on cross cutting relationships, it can be inferred that deformation occurred during and following the intrusion of the plutons of the same ages (Stevens et al., 1997). These structures include minor west verging structures in certain localities around intrusions, reactivated thrust and tightening of folds, rotation of SW-dipping cleavage and thrust faults to vertical or steeply dipping to the northeast, and the development of conjugate strike-slip faults (Stevens et al., 1997).

Sevier Thrust Belt formation began prior to 150 Ma in southeastern California as the inland response to subduction of Farallon plate, and emplacement of the Sierra Nevada, Idaho, and Coast Range batholiths (DeCelles, 2004). Basement thrust faults in the Clark Mountains are cross cut by plutons ranging in age from Late Jurassic to Early Cretaceous, indicating basement style thrusting occurred during the Sevier Orogeny (Walker et al., 1995). Pavlis et al. (2014) noted that younger, NW trending folds overprint these Sevier structures, suggesting a significant Laramide age overprint in the region.

The last episode of Mesozoic plutonism in east central California occurred in the Late Cretaceous. Crustal melting produced the highly evolved, two-mica granites that make up the Skidoo and Hall Canyon plutons of North and Central Panamint Mountains respectively, and the Kern Knob, Papoose Flat, and Birch Creek plutons farther west in the Inyo and White Mountains (Labotka et al., 1980; Stevens et al., 1997). Cobb (2015) confirmed that the two mica granites of the Panamint Range are part of this assemblage with a U-Pb data of 89 Ma on the Wildrose two-

mica granite. The contractional tectonism produced the Laramide Orogeny, and lasted through the end of the Cretaceous and into the early Cenozoic in places to the north as the convergent continental margin evolved into a transform boundary between the North American plate and the Pacific plate (Dickinson, 2004).

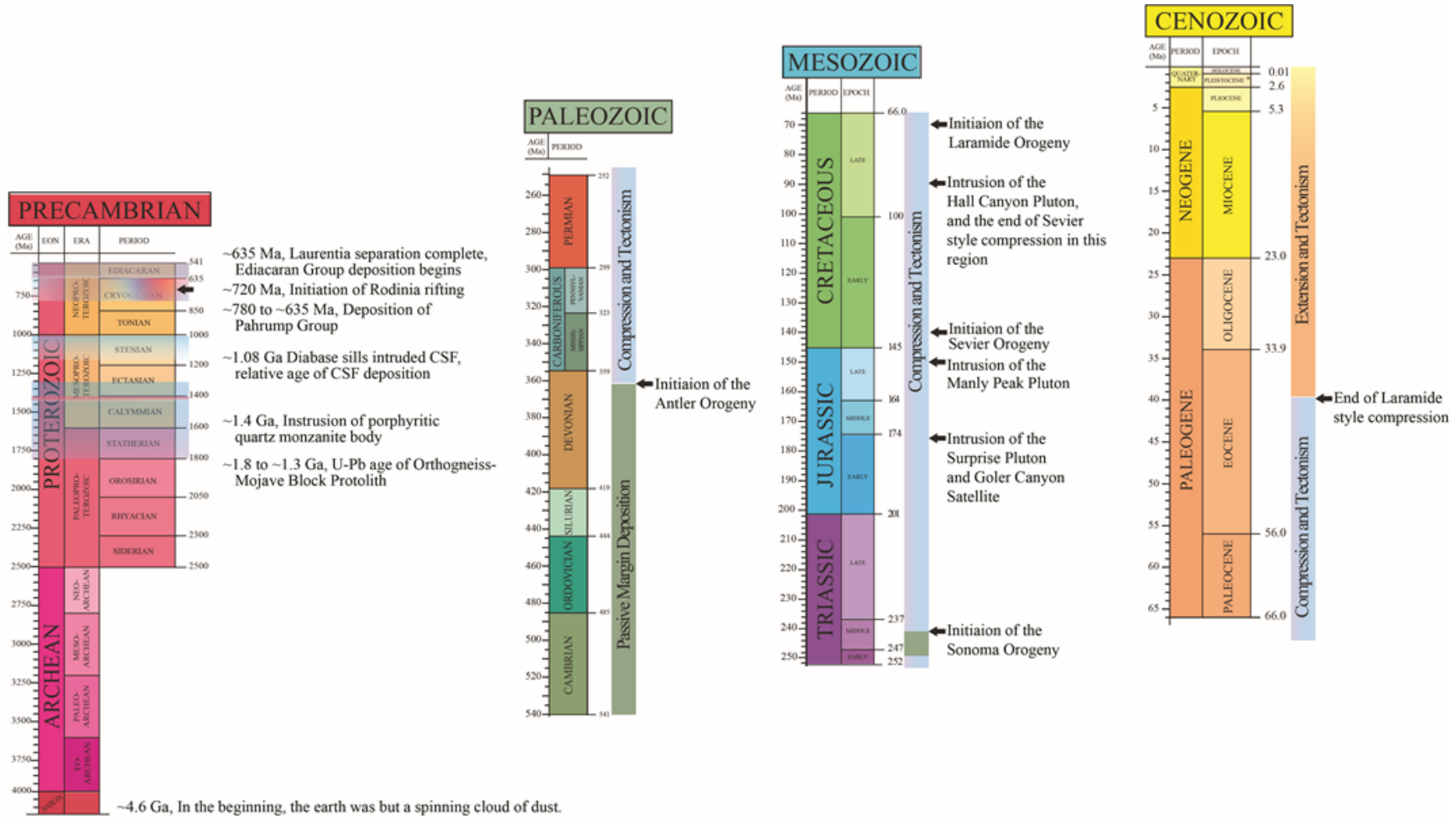

Figure 4. Timeline of Significant Events

METHODS

Due to the complexity of the geologic structures and rough terrain found in Surprise Canyon, multiple geologic tools and skillsets were applied. Digital mapping techniques allowed for the collection of detailed geologic data with a georeferenced tag. Light stable isotope chemostratigraphy produced a novel method to determine stratigraphic younging. Photogrammetry and 3D models helped to evaluate macroscale structures in the canyon walls. And uranium lead geochronology produced robust ages, allowing for further time constraints to be placed on Mesozoic deformation in the region.

FIELD WORK AND DIGITAL MAPPING TECHNIQUES

Digital mapping methods utilizing GPS enabled tablets and QGIS software were used to map central Surprise Canyon and a portion of Wildrose Canyon. This mapping was conducted at variable scales, typically >1:3,000 scales but with accuracy comparable to ~1:6,000. The mapping utilized a data structure similar to metamorphic projects described by Pavlis et al. (2010) modified for QGIS running on Dell or Asus tablets with the operating system Windows 8. All collected data were georeferenced with either a standalone i-Trek GPS unit paired to a Dell tablet or by Centrafuse Localizer software loaded on to an Asus tablet. The Centrafuse Localizer software utilizes the tablet GPS/GNSS device to provide location data via the tablet comport enabling the GPS tracking feature of the QGIS software. All shapefile linework was drawn directly onto pre-loaded satellite imagery and digital topographic maps obtained from the USGS (Pavlis, Langford, Hurtado, & Serpa, 2010).

Georeferenced orientation data was collected for compilation with previous work in Wildrose Canyon, western Surprise Canyon, and Pleasant Canyon by Brush (2015), Cobb (2015),

and Pavlis (2016) to build a kinematic history as described by stereonets. Using Excel, the data were sorted by location into planes and lines, and then further sorted by fabric generation and line type. The categorized data were then saved as individual comma separated value files. These were imported into Stereonet 10 and used to plot π-diagrams depicting data for deformation events D1 and D2 (Allmendinger et al., 2011; Cardozo & Allmendinger, 2013).

Georeferenced finite strain data collected includes mesoscopic *in situ* strain measurements, and shear sense estimates from minor structures. Long and short axes of stretched pebbles were measured on the surfaces parallel to foliation and perpendicular to lineation for ellipticity calculations $R_{X/Y}$ and $R_{Y/Z,}$ and max ellipticity. Boudinage was measured along the stretching axes in situ, from photographs using Adobe Illustrator, and from the photogrammetric model to calculate stretch (S = Lf/Li).

This study also used 3D mapping techniques using photogrammetric methods similar to those described by Pavlis and Mason (2017) and Brush et al. (2018). High visibility georeferenced ground control points were placed throughout key outcrops with spatial data recorded in the GCP_stations3D shapefile, and photographs were taken to build 3D photogrammetric models using Agisoft Photoscan software. The georeferenced camera positions were recorded in the Photo3D shapefile. Georeferenced marble samples were collected east of Limekiln Spring for isotope analysis. The obtained isotope trends in Figure 5 were compared to isotope composition values of the Beck Springs chemostratigraphy in Happy Canyon (Smith et al., 2016), and the

Noonday Dolomite chemostratigraphy in Wildrose Canyon (Petterson, et al., 2011).

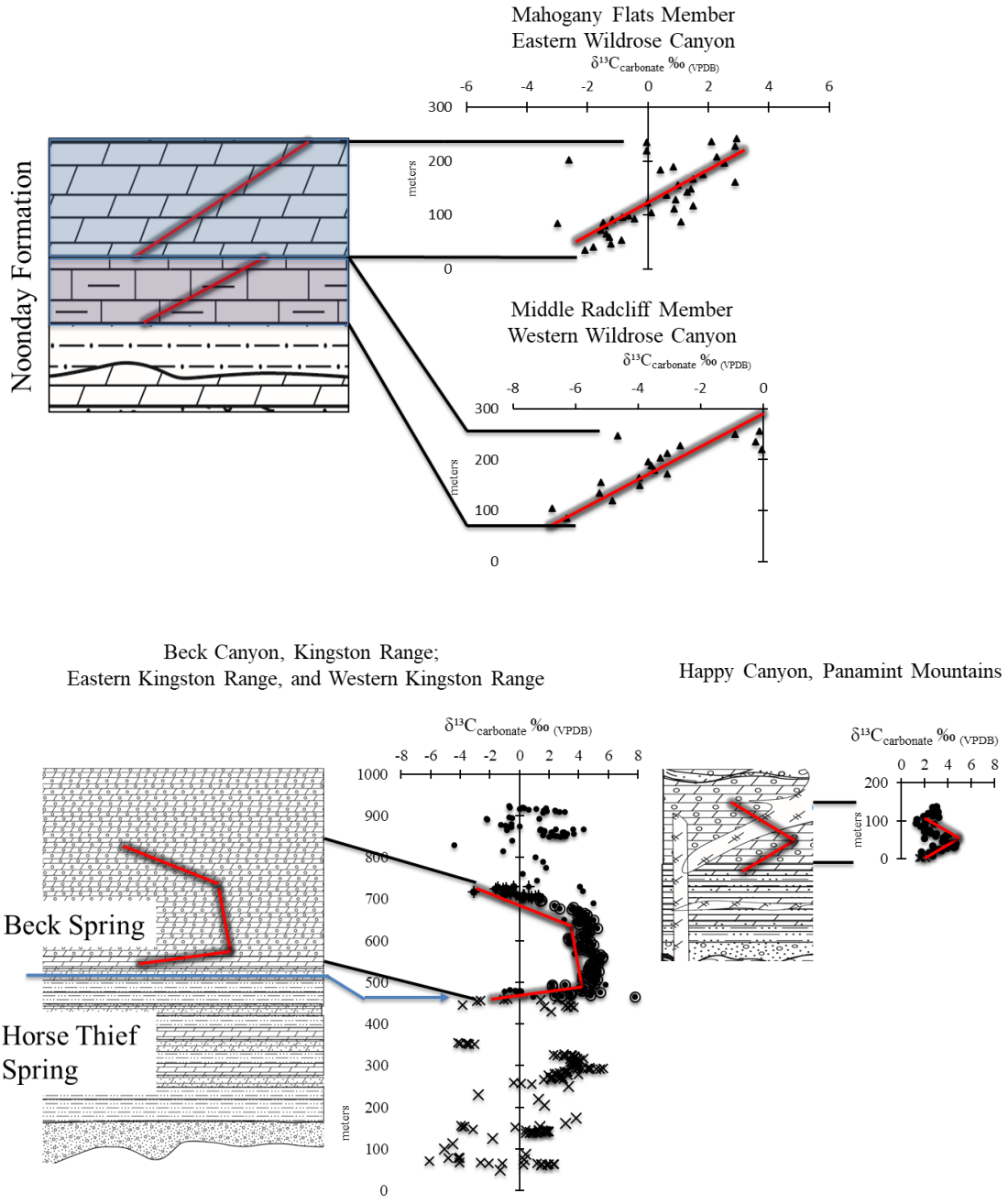

Figure 5. Chemostratigraphy of the Beck Spring Dolomite and Noonday Formation Compiled from Corsetti and Kauffman, 2003; Prave, 1999; Macdonald et al., 2013; Mahon et al., 2014; Smith et al., 2015.Compiled from Stewart, 1970; Wright et al., 1974; Labotka et al., 1980; Heaman and Grotzinger, 1992; Petterson et al., 2011. Red lines indicate best fit lines.

GEOCHRONOLOGY AND LIGHT STABLE ISOTOPE ANALYSES

Sample SPD18 was collected from a pluton of indeterminate Mesozoic age in Surprise canyon for analysis by a laser ablation multi-collector inductively coupled plasma mass spectrometer. The sample was collected from a boudinaged sill in the Limekiln Spring member of the Western Kingston Peak Formation. The sill is fully involved with the main D1 deformation, and the internal foliation is concordant with surrounding fabrics. The U–Pb and Lu–Hf isotopic analyses were done by multicollector laser ablation–inductively coupled plasma–mass spectrometry (LA–ICP–MS) at the Arizona LaserChron Center at the University of Arizona. The zircon U–Pb geochronology data were collected following the analytic methods described in Gehrels et al. (2008, 2009) and Gehrels and Pecha (2014), while Hf isotopic measurements were collected using the analytical methods described in Cecil et al. (2011) and Gehrels and Pecha (2014). The resultant U-Pb and Hf data were analyzed using the MS Excel plug-in Isoplot 4.15 to create concordia plots, weighted mean plots, and epsilon Hf plots.

Rock unit correlations of the deformed marbles in Surprise Canyon based on composition and fabrics are questionable because of the intense deformation of these units. The two likely candidates to which the marbles in Surprise Canyon belong, the Beck Spring Dolomite and the Noonday Formation both contain alternately interbedded mudstones and dolomites, and massive dolomite beds. In unmetamorphosed sections distinct sedimentary structures and mesoscopic appearance allow routine distinction of these units, but in metamorphosed sections both units are featureless, sugary white to grey marbles. In principle, stratigraphic order can also easily distinguish these units because the Beck Springs and Noonday Formations respectively underlie and overlie the very distinctive Kingston Peak Formation. Given the evidence in this region for isoclinal folding (e.g. Pavlis, 2012; Brush, 2015; Cobb, 2015) there is a high probability of large-

scale overturned sections, which renders stratigraphic correlations of marbles that are in contact with Kingston Peak Formation unreliable.

These issues led to a search for a more robust correlation of the marbles within this region. Fortunately, there is a wealth of chemostratigraphic and other geochemical data available from studies focusing on the Meso- to Neoproterozoic miogeocline sediments deposited on the western margin of Laurentia, specifically the carbonates. The carbon isotope compositions of the Beck Spring and Noonday formations display unique isotope values and trends which represent changes in the ocean water chemistry at the time of deposition (Fairchild & Kennedy, 2007) Figure 5.

The marble outcrops in Surprise Canyon with uncertain correlation are the 260-meter-thick, sugary white marbles east of Limekiln Spring, and the structurally higher marbles mapped as Beck Spring Dolomite outcropping around Panamint City, CA. Twenty-nine samples obtained from these sites were analyzed for their isotope composition together with marbles that were sampled west of Limekiln Spring by Pavlis during fieldwork in 2014, a piece of marble located in the Mormon Point turtleback in the Black Mountains, and a piece of the Sourdough Limestone collected from Wildrose Canyon during 2015. Powders for the analysis of the carbon isotope composition of the carbonate ($\delta^{13}C_{carbonate}$) were acquired by micro drilling of the collected rocks.

Once prepared, the carbon isotope composition of the micro-drilled rock powder was measured in-house using the continuous-flow isotope ratio mass spectrometry (CF-IRMS) at the newly established light stable isotope facility in the University of Texas at El Paso Department of Geological Sciences. For this reconnaissance analysis a fast procedure was used in which rock powders were combusted (for $\delta^{13}C_{carbonate}$) using an Elementar Pyrocube, followed by isotope analysis with an IsoPrime GeoVisION isotope ratio mass spectrometer. For carbon isotope

analysis, the powders were packed into tin capsules, and vanadium pentoxide was added as a catalyst. The combustion technique yields the carbon isotope composition of the bulk sample, i.e. it is the isotope composition of all carbon in the sample. This type of analysis can be used for the collected samples because there is essentially no organic carbon in these metamorphosed carbonates. Thus, any carbon obtained from these samples was sourced from the carbonate and does not give a mixed signal.

3D MODELS

Large scale, complex structures located in Surprise Canyon are well exposed in the steep and inaccessible canyon walls. This inaccessibility makes detailed mapping and sampling a challenge. Recent developments in 3D visualization and digital mapping techniques allow resolution of some of these complex structures. This study builds on the recent work of Brush (2015) and Cobb (2015) using these techniques to evaluate this complex structure.

Images of the north wall of Surprise Canyon were taken on two different days during field work in October 2016 to resolve the mesoscopic structures found in the marble east of Limekiln Spring. Ground control points of high visibility were placed where the terrain allowed, and were georeferenced with a conventional WAAS enabled GPS with spatial accuracies estimated at ~2m horizontal, ~7m vertical based on FAA requirements for WAAS corrected GPS. Images were taken in groups at different positions along the base of the outcrops located in both Surprise and Wildrose canyons. In Surprise Canyon, certain cliffs are more accessible which allowed us to gain about ca. 120 m of elevation to allow more vertical variations in imaging.

Lighting conditions were not ideal in October 2016. Thus, the images required exposure adjustments before the images were used for model development. This was accomplished using

Adobe Lightroom 2017. A new collection was created by importing the 315 JPEG images into the Library database. The images were then adjusted using 'Auto Tone' to adjust exposure, clarity, and saturation levels for 312 JPEG images. The artist brush tool was also used to strategically select areas of deep shadows or over-exposure for further correction via manual adjustment of the exposure, clarity, and saturation levels. These metadata masks were exported as XMP sidecar files with original the JPEG files into subfolders organized by outcrop location. Three images were not used due to lens flares.

The images were then imported into Photoscan as 'cameras' and separated into chunks based on outcrop location. The images within the chunks were further separated into camera groups based on the camera position in the canyon. The sky and dark shadows were masked out in Photoscan to prevent unnecessary points in the dense cloud. Through a batch process, the cameras were aligned, then optimized, and a low-density point cloud constructed. M*aptek I-Site Studio* was used to derive spatial data from lidar scans produced by Cobb (2015) to select ground control points (GCPs) for prominent and inaccessible features. Spatial data collected from ground control placed in the field was also loaded. As each ground control point was loaded, its location was verified in the images. The "Gradual Selection" tool under the "Edit" menu was utilized to remove extraneous points from the cloud. Once the GCPs were loaded and verified, another batch process was run to build a high-density point cloud, mesh, and texture. The texture model was then exported as *.obj. This file was then imported into *Maptek I-Site Studio* and the model was co-registered with the LiDAR scans taken by Pavlis and Cobb in 2013.

3D Mapping and Cross Section Building in Midland Valley Move

The regional digital elevation model was imported into Move as a raster file, and was loaded as a surface. Data from shapefiles containing contact and fault linework, orientation

measurements, and sample points were imported to the model and projected to the DEM surface using the "Project to Surface" tool in the build a model tab. Linework in the model was fused to the DEM surface as well.

Two cross sections were constructed with the Cross-Section tool under the Model tab by selecting a bearing 79º and designating a length of ten kilometers. Using the Project tool, fault, contact, and orientation data were projected on to the cross sections. Edit tools were utilized to alter line lengths, or rotate objects. Fault surfaces were modeled to ensure proper cross cutting relationships. Once editing was completed, polygons were created using contact and fault boundaries.

The georeferenced sample data points were imported into the model and projected to the DEM surface to derive elevation data. The sample points were then projected to the closest of four rough cross-sections to obtain a z-position with respect to the formation contacts. This z data was recorded in excel and used to build a chemostratigraphy column for comparison to compiled data from previous work by Smith (2015) and Petterson (2011), Figure 5.

RESULTS

DUCTILE FABRICS AND MESOSCOPIC STRUCTURE OF THE CENTRAL PANAMINT MOUNTAINS

In both Wildrose Canyon and Surprise Canyon the metamorphosed rocks are characterized by two prominent ductile fabric elements with fabrics decreasing in intensity in successively lower grade rocks. The most conspicuous fabric element is a prominent continuous cleavage (S1) with an equally prominent mineral (Lmin) or stretching lineation (Lext) developed on S1. Inspection of these fabric elements in areas with deformed objects (e.g. conglomerates) shows that the foliation

and lineation are coincident with the shape fabric, indicating that the main foliation is an accurate finite strain marker. Initiation of D1 deformation is loosely constrained by the ca. 176 Ma Surprise Pluton (this study). The main foliation (S1) is commonly overprinted by a crenulation cleavage (S2) that is associated with prominent folds (F2) in foliation. F2 mesoscopic folds are coaxial with observed map scale tight folds mapped by Albee et al. (1980) indicating these macroscopic folds are F2 structures, Plate 1 and 2.

D1 Deformation

The main fabric elements, S1 foliation and the intersection lineation Ls0-s1 were produced by the deformation event, D1. The original bedding, S0 was folded around NS trending F1 axes, mineral, and extensional lineations, L1. The close orientations of the best-fit π-circles to the poles of S0, S0=S1, and S1 foliations in both Wildrose and central Surprise Canyons are consistent with field observations of sub-parallel S0 and S1 due to D1 isoclinal folding, as described in western Surprise Canyon by Cobb (2015).

In Surprise Canyon, Figure 6, the S1 foliation poles scatter along a best-fit π-circle of 255º/82º, with the π-axis oriented at 166º/13º. The S0, S0 = S1 foliation poles scatter along the best-fit π-circle of 77º/77º with the π-axis oriented at 347º/13º. The majority of S0, and S0=S1 foliation data were collected east of Woodpecker fault and around Panamint City (Plate 1) where original bedding relationships within the Pahrump Group are preserved in a primarily east dipping structure. The primary D1 structure displayed west of Woodpecker fault is west dipping. These fabrics, Figure 6, are folded around the F1 axes poles cluster in a group east of south with a mean pole oriented at 169º/21º. The Ls0-s1 intersection lineations also cluster in the south with the Ls0-s1 mean pole oriented at 168º/10º. The π-axis of the poles to the F1 axial planes is oriented at 184º/17º.

In Wildrose Canyon, Figure 7, the S1 foliation poles scatter along a best-fit π-circle of 261º/87º, with the π-axis oriented at 171º/07º. The S0, S0 = S1 foliation poles scatter along the best-fit π-circle of 267º/89º with the π-axis oriented at 175º/02º. Both π-axes plot within the F1 axes trace, Figure 10. The F1 axes poles cluster in two north south groups, with the mean pole oriented at 173º/37º. The Ls0-s1 intersection lineations also cluster in two north south groups with the mean pole oriented at 169º/40º. The poles to the F1 axial planes scatter along a best-fit π-circle of 85º/83º, with a π-axis oriented at 355º/07º. The extension lineations have a mean pole of 173º/33º. The mineral lineations mean pole is 168º/22º. The overall structure is east dipping.

D2 Deformation

Formation of the secondary fabric elements record elements of D2. Cobb (2015) showed from cross-cutting relationships of a dated pluton that this fabric is post-89Ma. S2 foliation is a crenulation cleavage developed on S1 and is axial planar to open to tight, F2 folds. The related intersection lineation Ls1-s2 is parallel to F2, Figure 8 and 12. In both canyons, the π-axes to S0, S0 = S1, and S1 also plot within the scatter of the F2 fold axes and Ls1-s2 lineation intersections, which also scatter in a north-south grouping, similar to linear elements of D1. Poles to the main fabric element were plotted with the linear elements of the D2 fabric. Distribution of these poles relative to L2 linear elements suggest sub-cylindrical folding of S0, S0=S1, and S1 around F2 axes and NS trending linear elements in both Wildrose and Surprise Canyons. The S2 π-diagrams discussed below also support this conclusion.

In the deformation event D2 π-diagram of Wildrose Canyon data, Figure 8, poles to S2 foliations planes scatter in two opposing NW and NE clusters along a best-fit π-circle 106º/32º around the π-pole 178º/45º. The NW cluster is a much tighter scatter of shallowly plunging poles indicating steeply east-dipping fabrics. The NE cluster is a looser scatter with plunge of the poles

varying from steep to shallow. The variations could be attributed to natural scatter from measurement error, or more complicated W/NW dipping fabric. The Ls1-s2 lineation intersection mean pole is oriented at 164º/19º. The F2 axial plane π-axis is oriented at 003º/07º. The F2 axes mean pole is oriented at 39º/43º.

The Surprise Canyon S2 π-diagram, Figure 9, shows a similarly southeast dipping structure as in Wildrose Canyon, Figure 8. However, the S2 foliation poles scatter into NE/SW clusters. These plot along a π-circle of 73º/65º around a π-pole oriented at 343º/25º. The northeast grouping of poles with shallow plunges suggests steeply west-dipping fabrics, and the southwest fan of poles with plunges that vary from shallow to moderate implies a more varied northeast dipping fabric. The Ls1-s2 lineation intersection mean pole is oriented at 166º/15º. The F2 axial plane π-axis is oriented at 156º/11º. The F2 axes mean pole is 79º/41º.

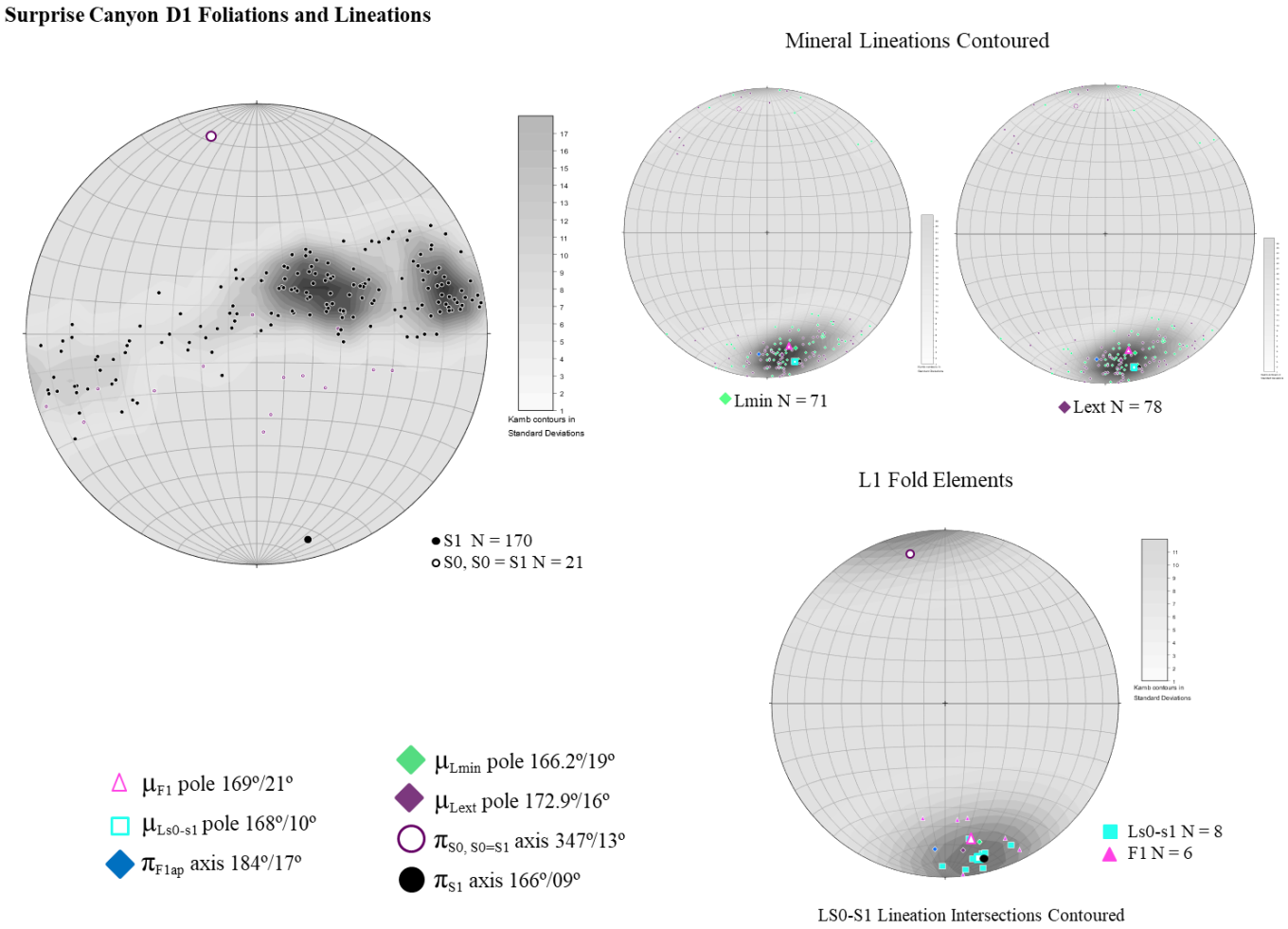

Figure 6. Surprise Canyon D1 Foliations and Lineations

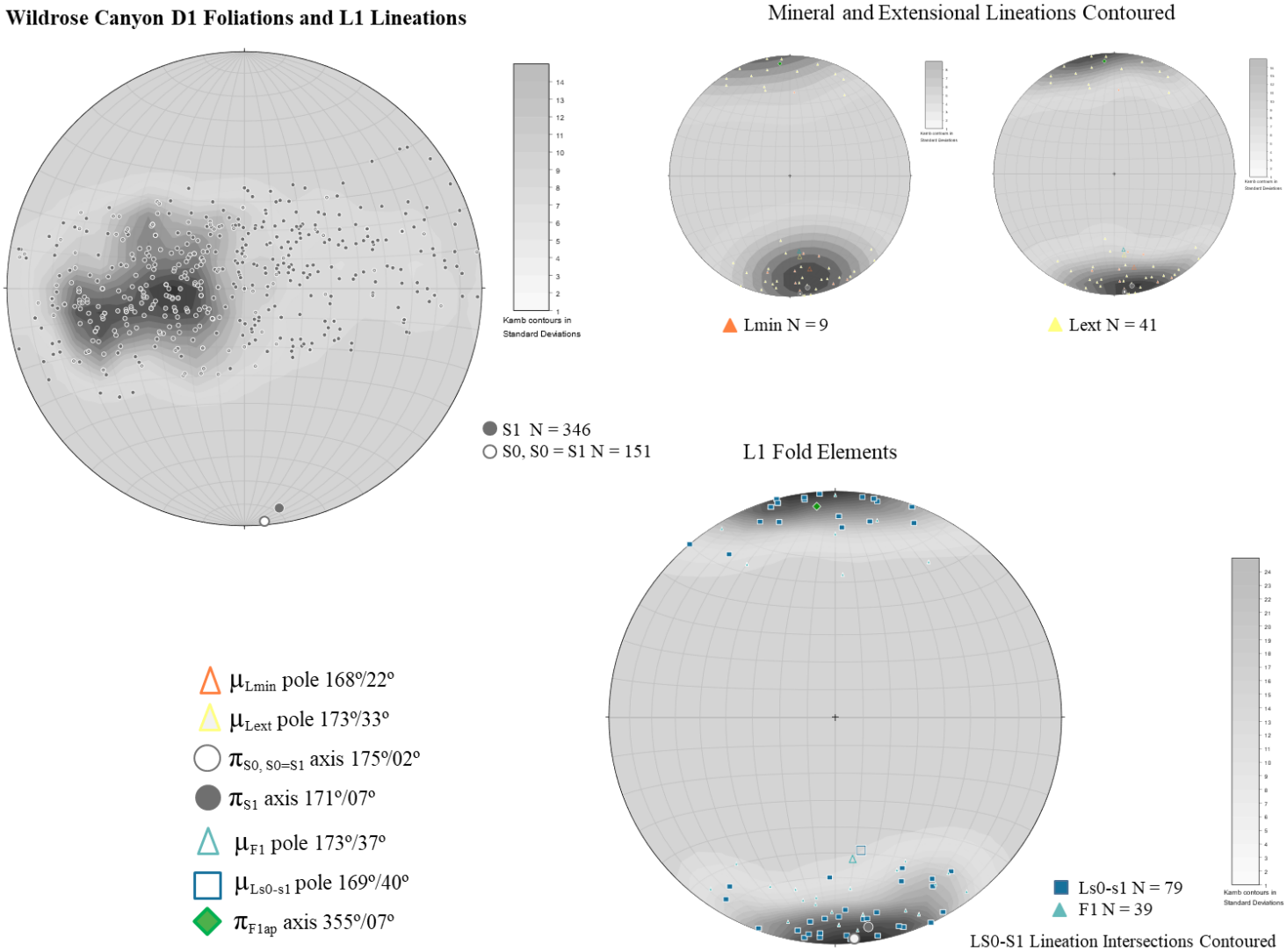

Figure 7 Wildrose D1 Foliations and Lineations

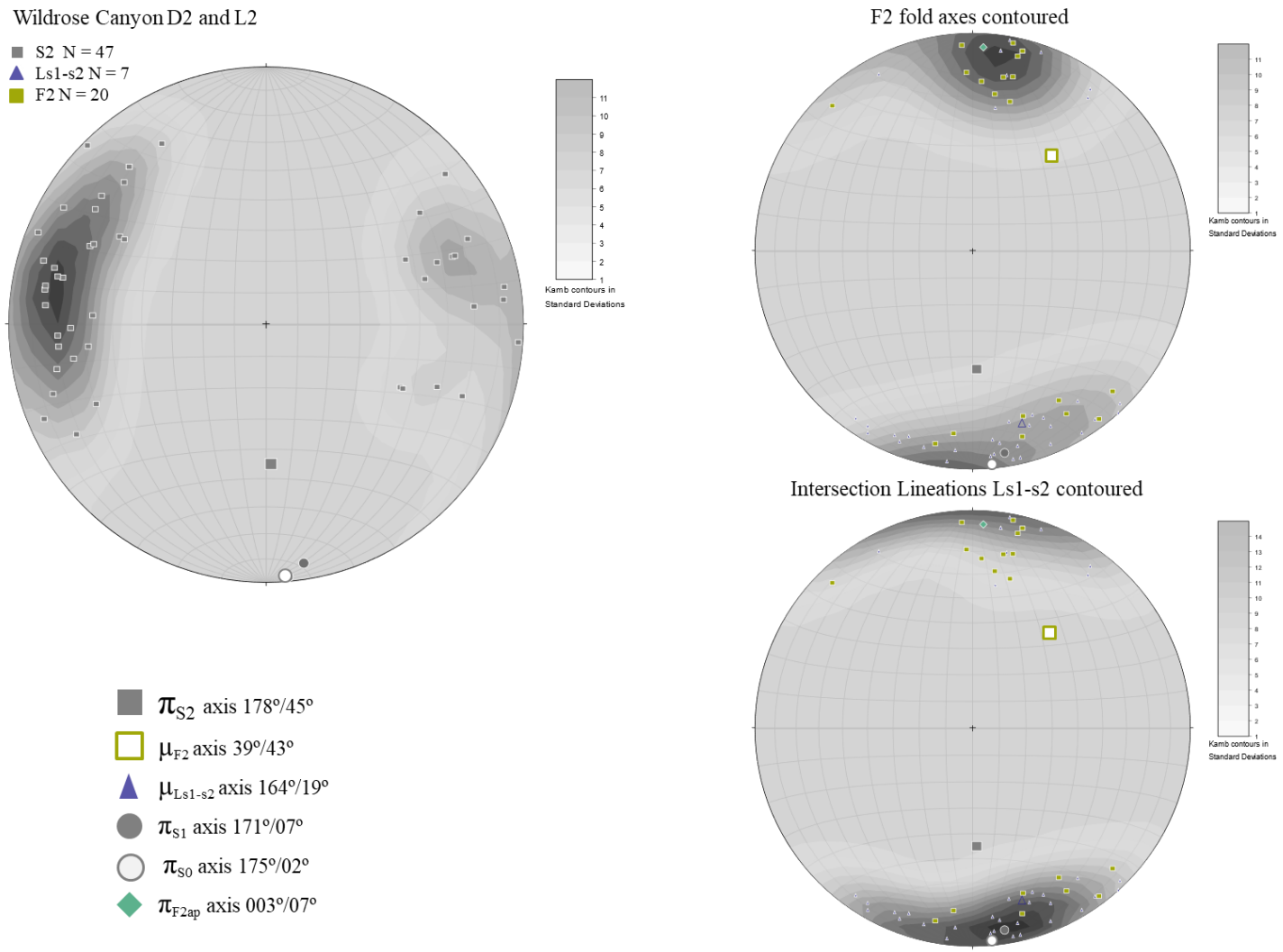

Figure 8 Wildrose Canyon D2 Foliations and Lineations

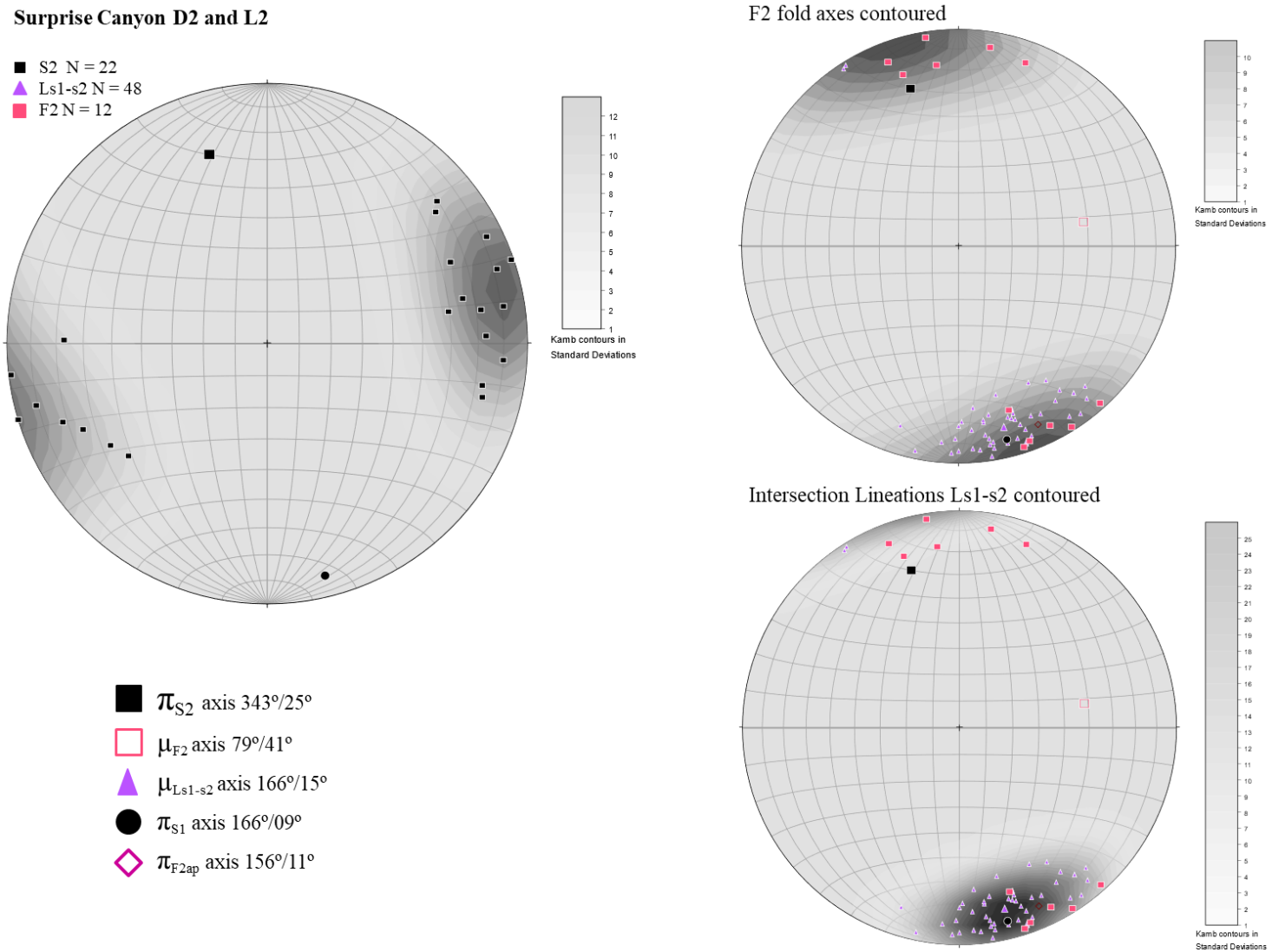

Figure 9. Surprise Canyon D2 Foliations and Lineations

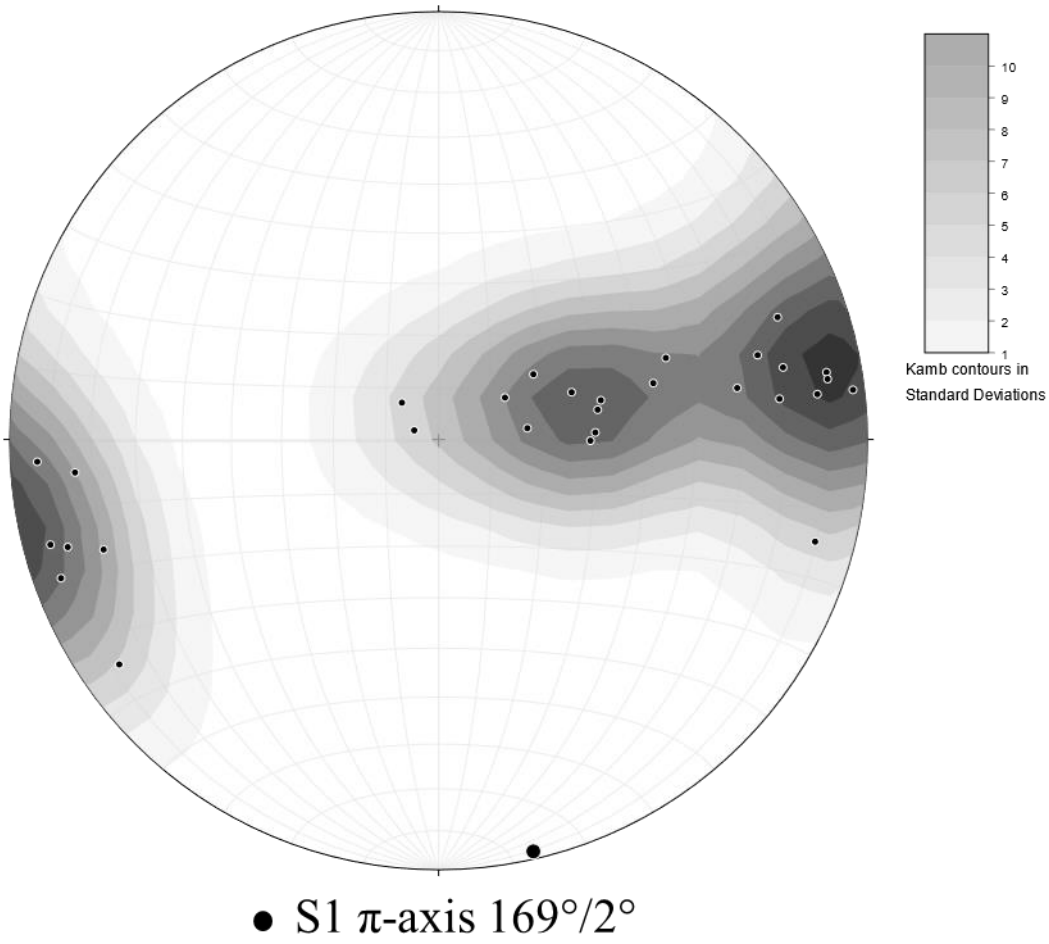

Figure 10. Brewery Spring Antiform Pi Diagram

KINEMATICS OF DUCTILE STRUCTURES

Finite Strain Estimates

Stretched Pebble Strain estimates

Strain measurements were made from stretched pebbles at 5 sites in the central Panamint Mountains with results shown as a Flinn Diagram, Figure 11. The measurements were made over a larger area than Plate 1 with one site in the Wildrose Diamictite exposed in Wildrose Canyon, sample 13WPA18 and the remainder from Surprise Canyon and Pleasant Canyon, including data from Cobb (2015) and Brush (2015). At all sites the pebbles show a NS elongation parallel to lineation. On the Flinn plot, the data indicate approximately plane strain to constrictional strain with X/Y or Y/Z ellipticities as high as 5, or maximum ellipticities (X/Z) approaching 25. The rocks with the highest strains (14JABPP and 14DP59) are both from lower surprise canyon, in the highest-grade rocks examined in this study. Note that the constrictional strain probably results from superposition of D1 and D2 strain with D2 shortening primarily in the foliation plane, perpendicular to lineation. Thus, D1 strains were probably approximately plane strain or potentially in the flattening field.

Boudinage Stretch Estimates

At several sites boudinage is prominent in the metamorphic complex. These include calc-silicate layers in marbles and metaplutonic sheets in schists or marbles. Where exposure allowed views perpendicular to boudin long axes it was possible to use boudin geometry to estimate the stretch, either by direct measurement with a tape or indirect measurement on photographs or photogrammetric models.

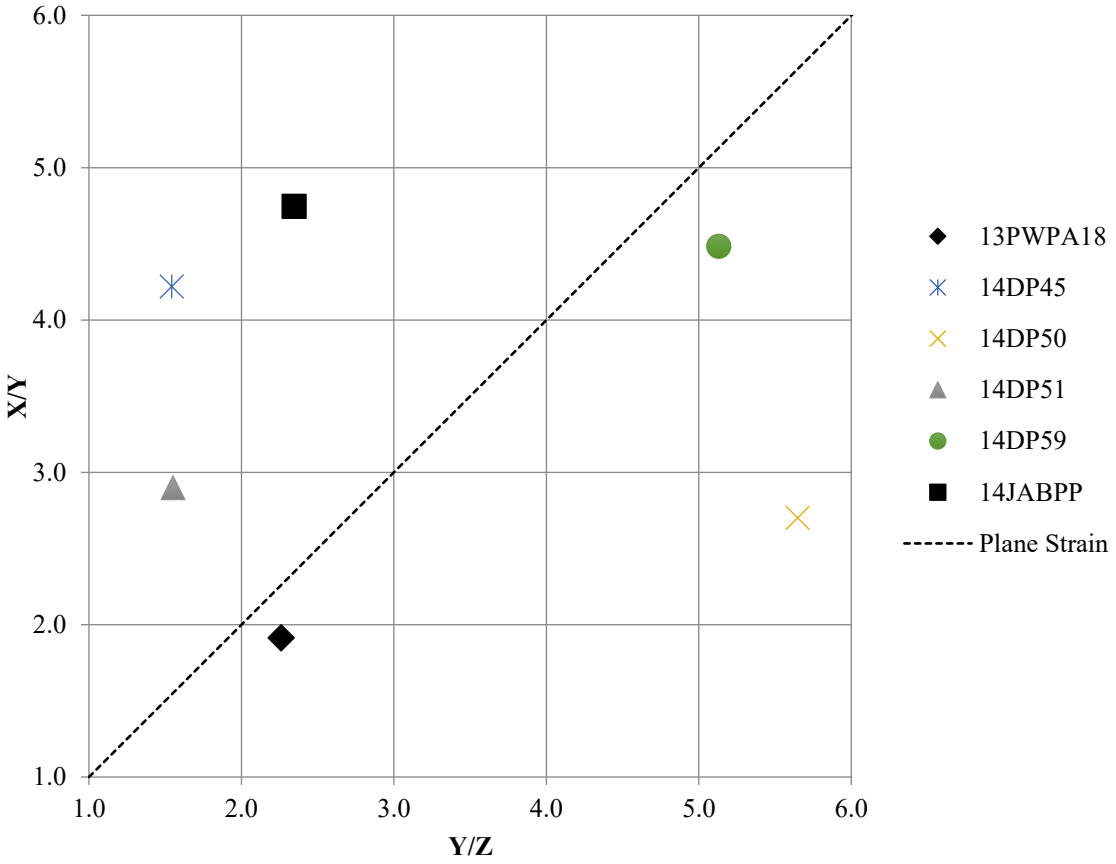

Figure 11. Flinn Diagram

Data compiled with Brush (2015) and Cobb (2015) strain measurements for comparison

Table 5 summarizes the results of these measurements. In all cases the boudin long axes measured are perpendicular to the stretching lineation, within the foliation plane, suggesting these measurements give a reasonable estimate of the stretching along the lineation axis. Total stretch estimates from this method range from 1.3 to 3.9 (Table 5). Using the photogrammetric model, the orange HTSM boudins were measured between 20 to 30 meters along Lext axis and show a stretch of 2, Table 5. In a tributary canyon in the south wall of Wildrose Canyon, an outcrop of the

Sourdough Marble displays chocolate boudinaged quartz lenses with stretch values of 1.6 to 2.2 along the NW stretching axis, and a stretch of 3.9 on the NE stretching axis, Table 5.

This range of stretch values is broadly consistent with the measured finite strain estimates. That is, assuming plane strain, the stretch along the Y axis is 1, and the boudin stretch values approximate the stretching axis, or the y axis (maximum stretch(X)/intermediate stretch (Y=1) of the Flinn plot (Figure 11). Thus, the range of values from 1.3- ~4 is consistent with observed finite strains. Note that this observation also is consistent with the conclusion that the bulk of the strain is pre-D2 because the boudinage structures show no clear association to D2 structure.

FIELD RELATIONSHIPS IN SURPRISE CANYON

Surprise canyon provides a nearly continuous exposure across strike from higher grade rocks exhumed from greater depths in the west to lower grade, and less deformed rocks, in the east. This provides an excellent perspective on variations in fabric development with structural level. Structural style varies along this transect. Thus, for clarity, the geology is described from west to east starting with the area surrounding Chris Wicht's Camp at the frontal fault zone, eastward to the Panamint city area (Plate 1).

The western flank of the central Panamint Mountains is covered by the Surprise Breccia, a monolithologic breccia derived from the Kingston Peak formation, and younger unconsolidated fanglomerates (Labotka, et al. 1980; Cichanski, 2000; Cobb, 2015). These late Cenozoic units comprise the hanging wall of a west dipping, low-angle range flanking fault associated with the Panamint Valley Fault Zone (Cichanski, 2000). The footwall rocks are comprised of Neoproterozoic units, and Mesozoic plutons. This fault surface is visible at the western end of Surprise Canyon at Chris Wicht's Camp (Plate 1). Here, a large amphibolite body associated with

the WKPF is exposed, along with the schist and greywacke beds of the Limekiln Spring member that has been correlated to the KP1 (Macdonald et al., 2013). This area displays large-scale isoclinal folds that were illustrated by Pavlis and Mason (2017). The amphibolite bodies, and folded schists and greywackes have been intruded by the Hall Canyon leucogranite that Cobb (2015) correlated to the Wildrose granite which he dated at 89.6 ± 2.2 Ma. Near the eastern edge of the leucogranite and ~200m up the southern canyon wall, there are small exposures of a highly deformed and boudinaged quartz diorite plutonic sheets in the greywacke of the Limekiln Spring member. This plutonic body was dated as a part of this study, and is referred to here as the Surprise Pluton.

Just above the leucogranite exposures in lower Surprise Canyon, Plates 1 and 2 (Appendix), is one of the most complex structural successions in the area. Indications of these complexities are the illogical juxtapositions of rock units noted by Cobb (2015). There are amphibolites related to the WKPF but hints of multiple generations of mafic rocks. Large mafic bodies form foliation parallel layers within the Precambrian orthogneiss unit, and the Crystal Spring quartzites and marbles consistent with the inference that some of the mafic rocks are deformed Paleoproterozoic intrusives seen regionally in basement and the Crystal Spring Formation. Amphibolites are also present, however, in the Limekiln Spring member of the WKPF as layer-parallel bodies with variable lateral extent (Plate 1). It is unclear if these units are metamorphosed flows, intrusives, or both, but they are clearly no older than the Neoproterozoic units that envelop them. Thus, in lower Surprise Canyon there are at least two generations of mafic rock.

A second stratigraphic complexity occurs along the southern canyon wall in lower Surprise Canyon (Plate 1). Here, and in a tributary canyon parallel along strike to the south, schists of the Limekiln Spring member lie on top of a diamictite/conglomerate unit, yet along strike to the north

the same schists lie against amphibolite and marble with no intervening conglomerate. Thus, the contact between the schist and underlying units is either a deformed, potentially angular unconformity, a deformed fault that is complicated by intrusion, or some combination of these.

Structurally below the Limekiln Springs member, to the east, the rocks appear to be a stratigraphic section (e.g. Albee et al., 1981) but in detail this interpretation is deceptive. There is an antiform in the foliation just west of Limekiln Spring, Plate 1, with orthogneiss in its core. On the west side of the antiform, referred to hence forth as the Drone Crash Antiform, foliation is subvertical with dips from steeply west to steely east reflecting a series of recumbent folds, but rolls to horizontal and gentle east-dips and steeper east-dips near Lime Kiln Spring (Plate 1). This observation led Albee et al. (1981) to show this structure as a simple anticline. In detail, it is much more complex. Above the anticline on the northern canyon wall, Plate 1, there is a brittle fault that truncates the vertical fabrics. This fault places a shallow-dipping allochthonous gray marble package that could be BSM structurally above a diamictite unit. This stratigraphic call would suggest the section is overturned above the fault. Alternate hypotheses are this package is the KP1 olistrosome and the marble is a large olistolith, or even a much higher stratigraphic unit like the Thorndike Limestone member of the upper Kingston Peak Formation. At present it is unknown which units occur in the fault hanging wall and further work is needed in this challenging terrain. Resolving these hypotheses is important because if the marble belongs to the Beck Spring Formation the overturning would require a large-scale recumbent fold dissected by the low-angle normal fault.

The east-dipping limb of the Drone Crash Antiform is truncated by a fault at Limekiln Spring, the Limekiln Spring Fault (LSF), Plate 1, Plate 2. The LSF is a normal fault that strikes north and dips steeply to the east, and juxtaposes the Beck Spring Marble in the downthrown block

above quartzites, amphibolite and carbonates that have been interpreted as Crystal Spring in the upthrown block. It is of note that this fault is the source of the Limekiln Spring, a tributary of Surprise Creek, with ground water presumably stopped by a permeability barrier at the fault.

East of the LSF is a prominent synform recognized in the original mapping of Albee et al. (1981) and described in detail by Cobb (2015). The west limb of the F2 synform is the east limb of the Drone Crash Antiform but across the LSF jumps up-section to a relatively clear stratigraphic succession of Beck Springs Marble (BSM), overlain by the Limekiln Spring Olistrosome, indicating a clear stratigraphic younging relationship. Albee et al. (1980) lumped this carbonate diamictite unit with the Limekiln spring unit, presumably because of this stratigraphic position. Nonetheless, it is of note that this basal portion of the Kingston Peak formation displays gross lithological differences from the rocks of the Limekiln Spring member just to the west, across the Drone Crash antiform. Thus, either there are unidentified structures separating the localities, or there are radical lateral sedimentary facies distinctions from east to west.

East of Albee's synform, the BSM is massive, ~260 meters thick. This increase in thickness of the Beck Springs marble is undoubtedly at least in part due to structural thickening, but stratigraphic variations are also possible. That is, given the complexity of the marble interpreted as Beck Spring surrounding Limekiln Spring-marble seen to the west, this contact could be a significant unconformity or a Precambrian fault.

To evaluate this problem further, a 3D photogrammetric model was constructed (Plate 3) of the contact between the marble and structurally underlying rocks to aid in the analysis of cryptic structural elements in this area. In the area of the model (Plate 3) the BSM is a massive white recrystallized marble that weathers to light brown. It displays a pervasive S1 fabric parallel to layering that has been folded around F2 fold axes and NS trending extension and mineral

lineations, Figures 6 and 9. Two west dipping faults crosscut S1 and have thickened the section, Plate 3. Five fault plane measurements were made using multipoint analysis of the faults on the 3D model using utilities in I-site studio, Plate 4. In visualizations of the 3D model it is apparent that the upper fault is truncated by the lower fault.

To the east, the unit below the marble is a mixed metaclastic-metacarbonate package of rocks displaying extreme boudinage of an orange carbonate layer. This unit is interpreted here as the Horse Thief Spring Formation, or normal stratigraphic order below the BSF. Below this layer is a brown marble, interpreted here as belonging to the middle Crystal Springs Formation. The marble and adjacent units are intruded by granodiorite that forms a sheet parallel to foliation and displays strong S1 fabric parallel to enveloping foliation. Fabric asymmetries in the granodiorite indicate top to the north shear sense. This granodiorite sheet is correlated to the Surprise Pluton based on shear sense and relative age. Below the granodiorite intrusion is a thick quartzite, tentatively correlated to the lower Crystal Springs. This quartzite unit is thick on the south wall of Surprise canyon, but limited to a thin layer on the north side of the canyon.

The east limb of Albee's F2 synform, Plate 2, is the west limb of an antiform that is referred to here as the Brewery Spring Antiform. The Brewer Spring antiform is truncated along its eastern margin by a prominent fault, the Woodpecker Canyon fault of Albee et al (1981), which separates rock of markedly different metamorphic grade and structural style. The Brewery Spring Antiform exposes gneissic rocks in its core, interpreted as Precambrian basement, overlain by a quartzite unit associated with brown marbles of the Crystal Springs, a marble-schist unit interpreted as Horsethief Springs Formation, and capped by the large marble unit interpreted as the Beck Spring Marble. Within the gneissic core, shear sense reversals were observed with tops to the north and

tops to the south moving up in elevation. The source of these contradictory shear-sense indicators is unclear but given the multiple phases of deformation in the gneissic rocks it is likely the product of fabric superpositions and not real reversals in shear sense. Like the Drone Crash Antiform to the west, unit thicknesses vary markedly around the antiform, presumably inherited from D1 fold systems that are difficult to resolve at this map scale. The core of the antiform also exhumes a highly deformed granitoid with foliation parallel to the enveloping gneisses. There is a normal fault that off-sets the granitoid with the downthrown block to the east. This metaplutonic rock is interpreted to be part of the Surprise plutonic complex based on its pre- to syn-D1 relative age.

Woodpecker Fault to Panamint City

Woodpecker Fault is a steeply west dipping structure that separates two metamorphic domains. To the west, the Pahrump group has been intensely deformed under amphibolite facies conditions to convert carbonates into a white, coarse grain marble, and produce an intense fabric in all of the rocks. East of the Woodpecker fault, however, the rocks are fine grained, and recrystallization is not prominent, even in meta-carbonates. The color of fresh surfaces of the Beck Spring Dolomite and Horse Thief Spring carbonates are dark grey, weathered surfaces are light blueish grey, and orange to dark brown, respectively. These observations are consistent with weakly metamorphosed rocks in eastern Death Valley. Moreover, layering dips moderately eastward in a simple, homoclinal structure to the eastern limit of the mapped area. However, there is a weak layer parallel (S0=S1) platey foliation in pelitic rocks of the Surprise Diamictite. The type section of the Kingston Peak Surprise Diamictite is exposed in this area and shows a weak S1 fabric with S0=S1 in areas, and internal fold structures in massive quartzites. All fabrics and layering are cut by the Tertiary Little Chief stock at the eastern limit of the mapped area (Plate 1).

CHEMOSTRATIGRAPHY

Light Stable isotope analysis of $\delta^{13}C_{carbonate}$ in twenty-three samples produced values that range from -2.5 ‰ to +3.5 ‰ with respect to VPDB. Midland Valley Move was used to project the georeferenced samples to a digital elevation map. These elevation positions were then projected to a cross section where stratigraphic position of each sample was estimated assuming a simple, stratigraphic section, Table 1 (Appendix). These positions were used to build a chemostratigraphy column (Figure 11). Samples from the marbles correlated to the Horse Thief Spring Formation produced $\delta^{13}C$ values ranging from -1.4 ‰ to +3.38 ‰. The marble samples from above the contact with Horse Thief Springs, presumably Beck Springs Marble, produced $\delta^{13}C$ values of ranging from +0.98 ‰ to +4.04 ‰. Samples collected from the metasomatized Horse Thief Spring Formation located in the far-east section of the canyon (1SP16, 2SP16, 6SP16, and 7SP16) produced $\delta^{13}C$ values of ranging from -2.66 ‰ to -1.40 ‰. Samples collected from the Horse Thief Spring Marble in the central section of the canyon (1SC16, 3SC16, 4SC16, and 5SC16) produced $\delta^{13}C$ values of ranging from +0.28 to +3.38 ‰. Samples collected from the metasomatized Beck Spring Dolomite in the far-east section of the canyon (13SC16, 14SC16, 15SC16, and 16SC16) produced $\delta^{13}C$ values of ranging from +0.98 ‰ to +3.38 ‰. Samples collected from the Beck Spring Marble collected from the central section of the canyon (2SC16, 6SC16, 8SC16, 9SC16, and 10SC16) produced $\delta^{13}C$ values of ranging from +2.79 ‰ to +3.46 ‰. Samples 11SC16 and 12SC16 were collected from eastern end of the canyon of the canyon.

Samples 14DP41 and 14DP42 were collected from the BSM, and 11SC16 and 12SC16 from the BSD. These samples were not plotted on the chemostratigraphy column due to the inability to estimate stratigraphic position due to the proximity of samples to faults, overturned bedding, and intrusive contacts. The $\delta^{13}C$ values produced of range from +1.44 ‰ to +2.75 ‰.

The rough chemostratigraphic column produced for Surprise Canyon produces a reverse C shaped curve that resembles the data curve of the chemostratigraphy column for the BSD type section in Beck Canyon of the Kingston Range (Smith et al., 2015). Thus, these data support the original stratigraphic interpretation of Albee et al. (1981) that these rocks belong to the Beck Springs formation. To make this data set more conclusive, future work could include a more detailed analysis of both the BSD in eastern Surprise Canyon, and the BSM in the central area of the canyon. Nonetheless, there is little evidence that these marbles were derived from the Noonday dolomite due to its very different C isotope signature.

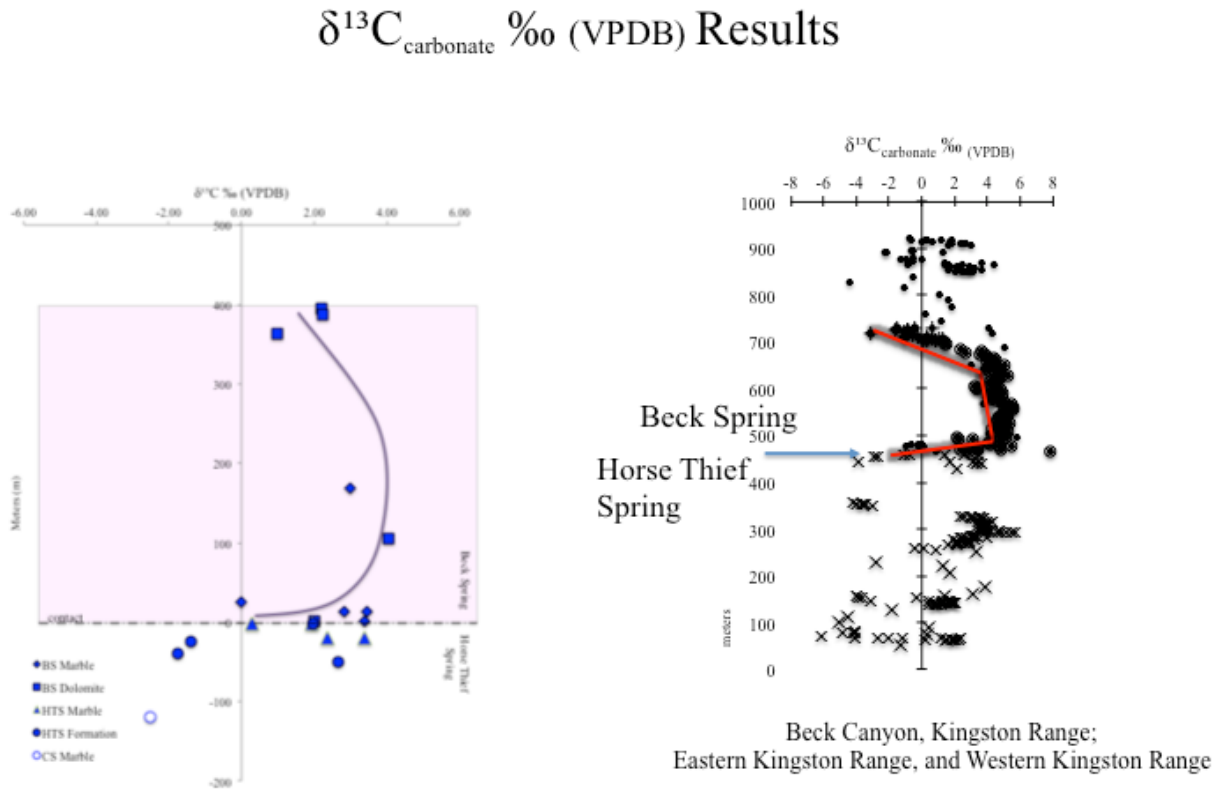

Figure 12. Light Stable Isotope Chemostratigraphy Of Surprise Canyon Carbonates. Zero on the y-axis marks the contact between the Horse Thief Spring Formation and the Beck Spring Dolomite

GEOCHRONOLOGY

LA-ICP_MS of Zircon U-Pb Isotopes

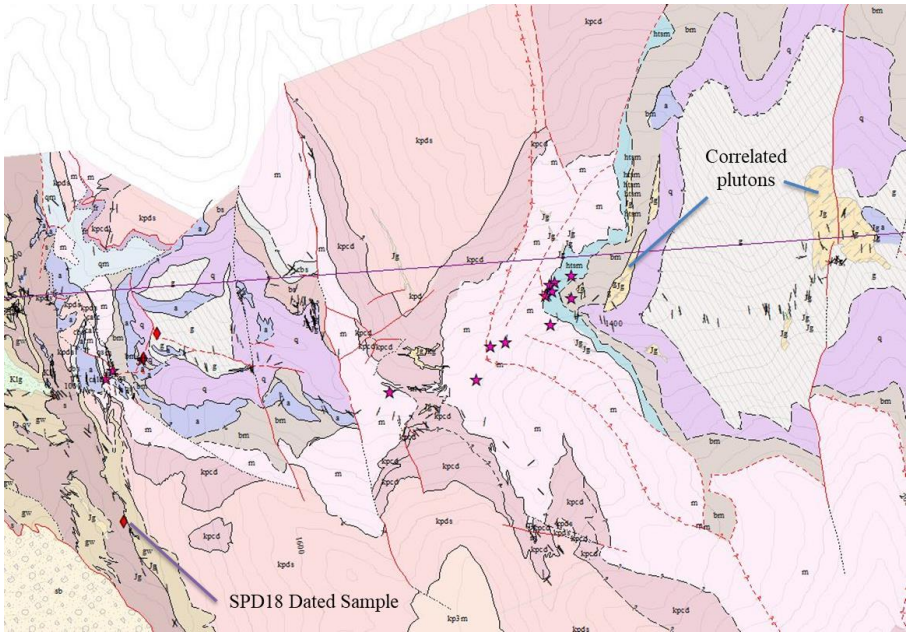

Figure 13. SPD18 Sample Location and Correlated Plutons

Zircon grains were collected from a sample of highly deformed quart diorite/granodiorite in lower Surprise Canyon (SPD18), Figure 13. Zircons are an 80/20 mixture of fragments and whole grains of lengths that range in size from 100 µm and 300 µm. The morphology of the zircons varies from euhedral and sub-euhedral with forms ranging from {101} and {101} vs. {110} to subrounded, xenocrystic grains indicating growth in an igneous environment. The grains are zoned; some oscillatory, others with more complex patterns. Many display resorption rings with an overgrowth rim ranging in thickness from 1µm to 10µm, Plate 5.

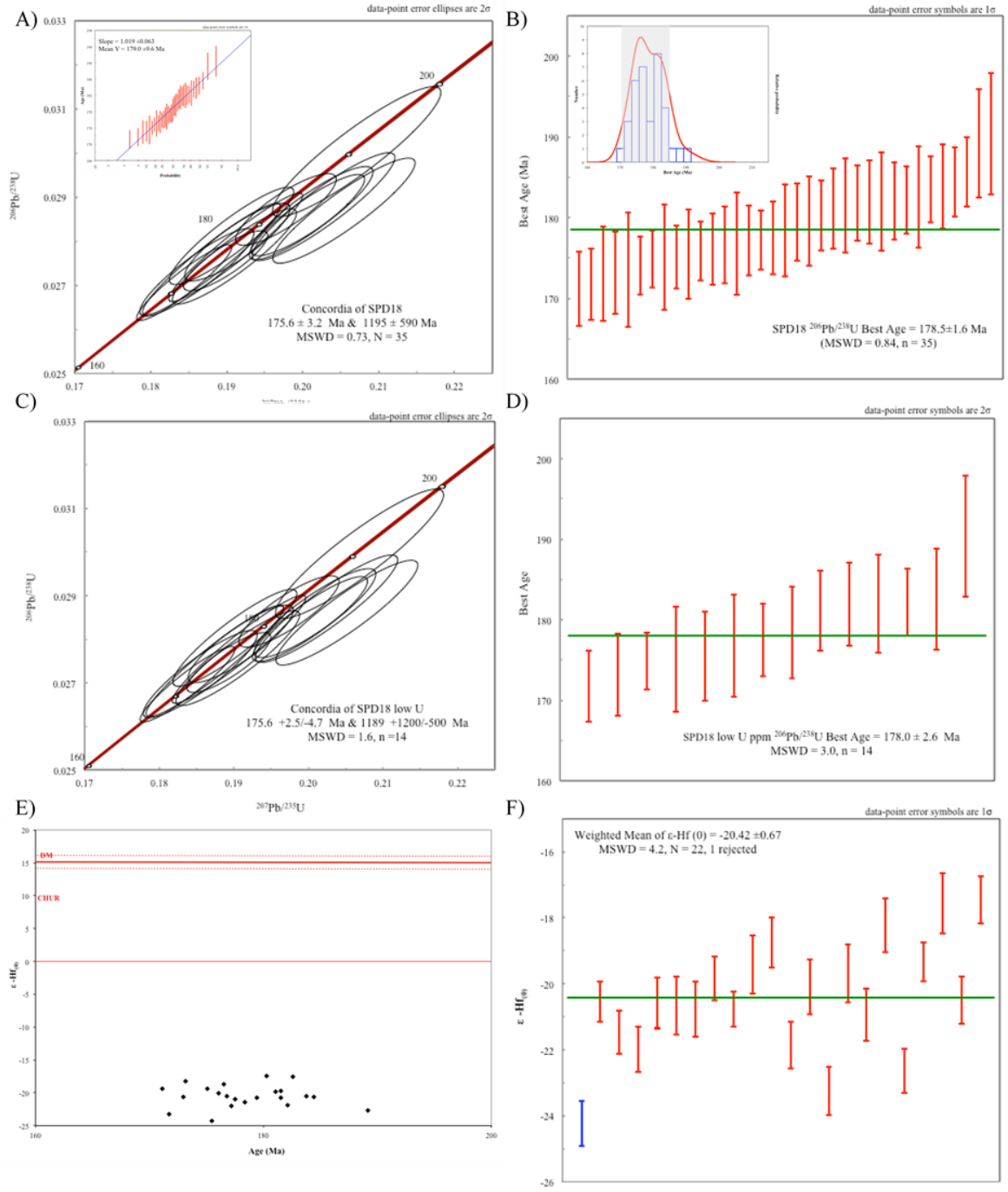

Figure 14. Geochronology Statistics of SPD18

A - Concordia of entire zircon population, high U ppm data ellipses are dotted lines, inset is linear probability plot. B – Weighted mean of best ages for entire zircon population, inset is probability density histogram. C – Concordia of dates with uranium concentrations <1000 ppm. D – Weighted mean of best ages with uranium concentrations <1000 ppm. E – Epsilon plot of hafnium data. F – Weighted mean of ε-Hf (0) values.

U-PB zircon analysis was performed on twenty-one zircon grains with thirty-five spot

analyses, which produced coherent data, Table 2. SPD18 U-PB DATA The resultant $^{207}Pb/^{206}Pb$ dates range from 171.1 ± 4.6 Ma to 190.8 ± 7.7 Ma (Figure 14). A weighted average of all $^{206}P/^{238}U$ dates produced a weighted mean date of 178.5 ± 1.6 Ma, and an MSWD value of 0.84, and an uncertainty ~1σ (Figure 14b). All dates range in concordance from 99% to 104% with an average of 101%. When plotted on a concordia diagram (Figure 14a) the data are broadly concordant but form a weak discordia line with an upper intercept at 1195 ± 590 Ma and a lower intercept at 175.6 ± 3.2 Ma and an MSWD value of 0.73, and an uncertainty ~2σ. Uranium concentrations in the grains range from 357 ppm to 5907 ppm with an average of 2614 ppm. Thorium concentrations range from 157 ppm to 10770 ppm with an average of 2769 ppm. U/Th ratios are consequently low ranging from 0.5 to 12.3 with an average of 1.6. The inset probability density plot in Figure 14b displays a peak at ~176 Ma, and the inset linear probability plot line in Figure 14a has a slope = 1.019 ±0.063, and a mean Y = 179.0 ±9.6.

In Figure 14c-d, high uranium concentrations, greater than 1000 ppm, were excluded from the weighted mean and concordia plots to show the consistency of the data, leaving a sample of fourteen. The weighted average of the fourteen $^{206}P/^{238}U$ dates produced a weighted mean date of 178.0 ± 2.6 Ma, and an MSWD value of 3.0, and an uncertainty ~2σ. This age estimate is within error of the lower intercept of 175.6 +2.5/-4.7 Ma on the Concordia plot (Figure 14a) indicating igneous age of the sample is on the order of 176-179Ma, which is Early Jurassic. Because this sample was collected from a boudinage plutonic body that is fully involved in D1 deformation, this date represents is either pre-D1 or synchronous with the earliest phases of D1 deformation.

Zircon Lu-Hf Isotopes

In Figure 14e-f, the weighted mean zircon initial Hf isotope compositions were calculated

at the crystallization ages of the pluton sample with an uncertainty of ~1σ. Twenty-two analytical spots were measured for Lu and Hf on fourteen zircon grains from SPD18 and yielded negative ε-$Hf_{(0)}$ values ranging from -17.5 to -24.2 and adders from 0.6 to 0.9, and negative ε-$Hf_{(t)}$ values ranging from -13.8 to -20.6. Spot ages reported range from 171 Ma to 189 Ma. The weighted mean of the negative $\varepsilon Hf_{(0)}$ values is -20.42±0.67, an MSWD value of 4.2, and an uncertainty ~1σ. The weighted mean of the negative $\varepsilon Hf_{(t)}$ values is -16.92 ± .74, an MSWD value of 5.3, and an uncertainty ~1σ. The majority (72%) of yielded negative εHf-(t) compositions range from -15.1 to -18.8. For complete U-Pb and Hf analyses results, see tables x and y. These values are within typical ranges of granitoids found in arcs developed on old, Precambrian crust (Andersson, Högdahl, Sjöström, & Bergman, 2006).

DISCUSSION

KINEMATICS AND HISTORY OF DUCTILE DEFORMATION IN THE CENTRAL PANAMINT MOUNTAINS

Detailed mapping in Surprise Canyon together with strain estimates and fabric observations indicate that two phases of ductile deformation have produced variable fabrics that indicate increasing finite strain with increasing structural depth during the deformation. In the deepest structural levels, in lower Surprise Canyon, a prominent schistosity with a strong NS trending stretching lineation is present in rocks with the highest measured finite strains. In contrast, in upper Surprise Canyon, fabrics become less prominent with a simple layer-parallel phyllitic cleavage and uniform, homoclinal east-dipping layering. This strain gradient was produced during two phases of ductile deformation with the first (D1) undoubtedly producing the bulk of the finite strain

and the second (D2) producing the prominent upright folds in foliation (F2) seen at outcrop to map scale and associated with local development of a crenulation cleavage (S2).

Shear sense indicators are recognizable in scattered localities throughout the Central Panamint mountains. However, the data are limited because the D2 overprint generally obscures these features. Nonetheless, aside from shear sense reversals seen while moving up in elevation through the Brewery Spring antiform, clear shear sense indicators elsewhere show a consistent pattern of top to the NNW. Given the measured finite strains that scatter along a plane strain line, Figure 11, this suggests D1 strain was dominated by simple-shear plane strain.

The cross-section AA' has a bearing of 79° perpendicular to the stretching lineation. In Plate 2, the cross-section is rotated 20° counter-clockwise to restore horizontality to the eastern tilted stratigraphy located at the east end of Surprise Canyon. This rotation is likely a minimum, however, because Cenozoic strata along the eastern margin of the Panamint Mountains dip 30-40 degrees east (McKenna and Hodges, 1990), suggesting the entire Panamint Mountain block experienced this rotation. After this rotation, the fabrics west of Woodpecker Fault dip moderately to steeply west, Plate 2b. This observation is important for two reasons: 1) after restoration, F2 folds are west vergent, a relationship distinct from east-vergence generally associated with late Mesozoic contraction; and 2) the prevalence of top-north shear senses in D1 structures that restore to relatively steep dip suggests D1 may record ductile, dextral strike slip motion. .

The Woodpecker Fault crosses an important transition in the metamorphic fabrics in Surprise Canyon and complicates the original and simple interpretation of this transition. Specifically, although an important objective of this study was to evaluate the evidence for the Harrisburg Detachment fault, the Woodpecker fault occupies the equivalent structural position of the structure as mapped by McKenna and Hodges (1990). Thus, more data in the area surrounding

Woodpecker Fault, particularly tracing the fault northward from Surprise to Hall Canyons, is needed to better determine the nature of the fault and to better resolve the strain gradient where the fault is less significant.

LIGHT STABLE ISOTOPES

This study attempted a reconnaissance investigation using light stable isotopes as a fingerprint for distinguishing marbles in the stratigraphic section. The simplest application of the method successfully showed that the stratigraphy, as originally mapped, was probably correct because of the distinctive general isotopic signatures of the Beck Spring Dolomite and the Noonday Formation carbonates. Although the method was helpful, it could give misleading answers as well. If units are isoclinally folded, then the shape of the chemostratigraphy curve could be reflected, inverted, or reversed, in the upper limb of the fold. In some ways this could be helpful in identifying stratigraphic up given the illogical juxtapositions found in the lower canyon. There are limitations with chemostratigraphy measuring methods in Surprise Canyon due to the steep and mostly cliffy terrain of the canyon, and the subsequent need for well-trained climbers and climbing gear for the purpose of safe and effective sample collection.

ABSOLUTE AGE CONSTRAINTS ON THE DUCTILE DEFORMATIONAL HISTORY

Sample SPD18 provides the first clear maximum age for the bulk of the ductile deformation in the Panamint Metamorphic complex. This plutonic body is fully involved in D1 indicating most, or all, of the ductile deformation occurred after the ~176 Ma intrusion of this body. Correspondingly, a minimum age for D1 is provided by Cobb's (2015) date on the post-D1 Wildrose leucogranite at ~89 Ma. Unfortunately, although these age data provide a clear constraint,

this age range could have been deduced from regional geology. Fortunately, other information is available.

Cobb (2015) reported three U-Pb zircon dating results from syn-tectonic plutons in lower Surprise Canyon that can be reevaluated in light of the results from geochronology data collected from SPD18 (Table 2 and Plate 5). In Cobb's (2015) study, spot analyses yielding Early Jurassic dates and robust concordia were dismissed due to high uranium concentrations and extensive scatter in the data on a Concordia plot. The samples are summarized below and presented in geographic order from west to east, Plate 1, to consider this problem.

Sample 14DP53 is from a boudinaged syntectonic pegmatite sill located on the southern wall of the canyon, above and to the east of Chris Wicht's Camp (Plate 1). Fifty-one spot analyses were performed on forty-nine zircon grains, however only four of these analyses produced coherent data due to uranium levels exceeding the faraday collector capabilities. Two grains with distinct inherited cores produced $^{206}Pb/^{207}Pb$ dates of 1328.1 ± 9.5 Ma and 1775.9 ± 12.7 Ma with respective low uranium concentrations of 151 ppm and 115 ppm, and Th/U ratios of 0.52 and 0.54. Two grains with spongy textures returned younger $^{206}Pb/^{238}U$ dates of 180.5 ± 12.0 Ma and 181.3 ± 2.6 Ma with respective uranium concentrations of 2314 ppm and 1805 ppm, and Th/U ratios of 0.015 and 0.016. The Meso- and Paleoproterozoic cores indicate preserved cores from anataxis of the basement protolith, but the Early Jurassic metamict grains probably represent zircons precipitated from a hydrothermal aqueous fluid associated with the metamorphic event (Cobb, 2015). The similarity of these ages (~180Ma) to SPD18 (~179Ma) supports this conclusion.

The last two samples were collected from the core of the Drone Crash Antiform core near Limekiln Spring. Sample 14DP52 was taken from a leucogranite dike that cross cuts the quartzite interpreted as lower Crystal Springs Formation on the southern wall. Fifty-nine spot analyses were

performed on fifty-one grains, with thirty-two analyses providing coherent data. Most of the grains returned $^{206}Pb/^{207}Pb$ dates from the Meso- and Paleoproterozoic and uranium concentrations less than 700 ppm. One grain with a spongy texture and a uranium concentration of 875 ppm provided the $^{206}Pb/^{238}U$ best age of 202.7 ± 5.5 Ma. Cobb proposed a hypothesis that the Proterozoic grains were detrital zircons sourced from the CS Quartzite that were recrystallized and assimilated into the leucocratic dike during the time of intrusion in the Earliest Jurassic. Thirteen spot analyses of the grains in this sample returned uranium concentrations that exceed the faraday collector capacity of 3100 ppm. The $^{206}Pb/^{238}U$ best ages for these spot analyses range from late Cambrian to Early Triassic. However, the $^{206}Pb/^{207}Pb$ best ages range from ca. 187 Ma to ca. 200 Ma, with one early Permian outlier. The relatively tight scatter of the much younger $^{206}Pb/^{207}Pb$ ages compared to the wide $^{206}Pb/^{238}U$ ages is also compelling. Thus, although this pluton should be re-evaluated, the results strongly hint that this rock, like SPD18, is Early Jurassic, circa 180 Ma.

Sample 14JGSC5 is perhaps the most revealing of these samples, Figure 15. This sample was taken from the mylonitic orthogneiss exposed on the northern wall within the Drone Crash Antiform, and was considered by Albee et al. (1981) as Precambrian basement. The mapping reported here (Plate 1) is also consistent with that interpretation of protolith. Forty-six analyses were made on sixty grains, and twenty-nine of these analyses produced coherent data. This sample included a population of Paleoproterozoic grains, late Paleozoic grains, Late Triassic grains, Early Jurassic grains and one Middle Jurassic grain. Cobb concluded the orthogneiss had undergone a metamorphic event during the Late Triassic and Early Jurassic.

Although Cobb's (2015) data alone is relatively ambiguous because of complexity in the U-Pb system for his samples, the data can be interpreted in light of results for SPD18 (Figure 14).

All three samples show extensive inheritance in zircon cores, but all at least yield some rim ages in the ~180 Ma range. Given that 14JGSC5 is appears to be from metamorphosed basement rock, this implies that the actual age of prograde metamorphism in the area was Early Jurassic and the rim ages represent metamorphic overgrowth ages.

Although these observations are intriguing, the conclusions for Early Jurassic metamorphism is tentative. Future work needs to address the age of metamorphism in the Panamints more precisely, either through more work on U-Pb dating of syntectonic plutons where high U contents are not a problem, or using other techniques for directly dating the metamorphism. In any case, the data reported here, together with Cobb's (2015) data leave no doubt that all of the ductile structure in the Surprise Canyon area is Mesozoic. Given the similarity in structural styles between Surprise Canyon and observations by Hodges et al. (1987) at Tucki Mountain, this conclusion places significant doubt on interpretations that much of the structure at Tucki Mountain is Neogene (Hodges, et al., 1987)

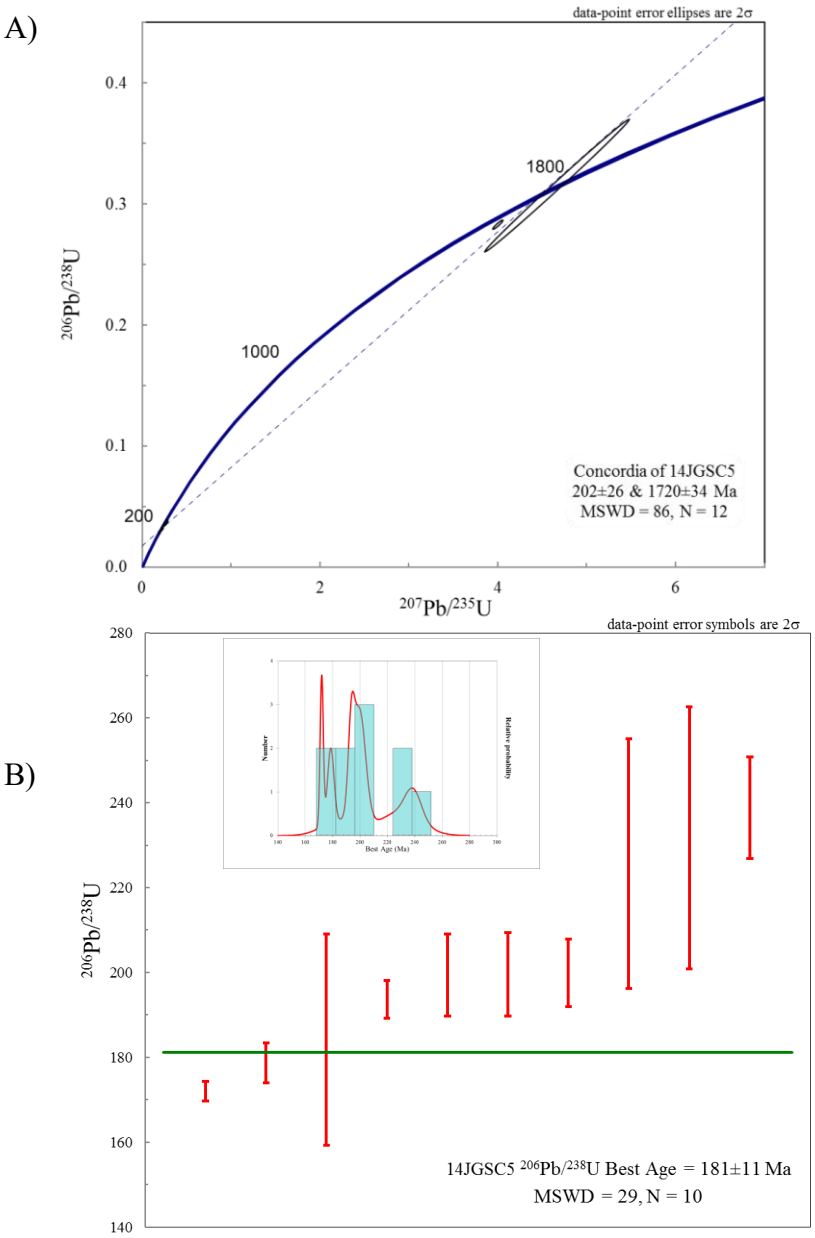

Figure 15. A. 14JGSC5 Concordia and Weighted Mean Plots

Late Triassic and Early Jurassic dates, plus two Mesoproterozoic dates. B.14JGSC5 206Pb/238U Best age is the mean of Late Tr and Early J dates only, and probability density plot inset. Selection of dates was based on age range and no more than 5% discordant.

CONCLUSIONS

The Central Panamint Mountains have undergone three metamorphic events, with the initial event occurring around the time of the intrusion of the Surprise Pluton during the Early

Jurassic. Interpreting this date as the primary prograde event explains the pronounced strain gradient and intense recrystallization of the marbles associated with the Lower Pahrump Group observed in western and central Surprise Canyon. Hafnium data indicates the pluton magma was sourced from continental crust, and high uranium concentrations found within the zircons indicate the melt source contained uranium rich minerals. The Early Jurassic date of the pluton also gives a clear maximum age for the bulk of the ductile deformation in the Panamint Metamorphic complex that occurred during deformation event D1.

With the new maximum age, this study is able to constrain deformation event D1 from post 176 Ma to 89 Ma, the date for the Wildrose pluton produced by Cobb (2015) based on cross cutting relationships. Two orogenic events that caused deformation in the region at that time are the Eastern Sierra Thrust System and the southern section of the Sevier Thrust Belt. Finite strains recorded in the area are likely related to the Sevier Orogeny, however there could be some transfer of stresses that occurred between the systems. More work is needed here to confirm this hypothesis. It is possible that during D1, the Pahrump Group marbles in the Panamint block took up a lot of the strain from the deformational stresses related to these Middle Jurassic orogenic events.

Strain markers, fabric geometry, and limited shear sense indicators indicate D1 was likely a plane-strain simple-shear dominant event with a top to the north sense of shear. When Neogene range tilt is restored, D2 structures show west vergence and if that shortening were restored, the main fabric development (D1) was likely a dextral strike-slip event. This hypothesis needs further assessment, however, as shear sense indicators are limited and there is, as yet, insufficient data to clearly restore D2 structure.

Using chemostratigraphic curves to identify metamorphic rocks that retain primary stratigraphy can be useful. However, if isoclinal or other expressions of intense folding or faulting are present, this could complicate and distort the chemostratigraphy signature pattern displayed in the column. In this study, the overall contrast in the isotope composition of the two options for carbonate bodies, the Beck Spring Dolomite and Noonday Formation facilitated the assignment of a metamorphosed carbonate unit the Beck Spring Dolomite. The photogrammetric models helped to see the macroscopic scale of the D1 extensional structures preserved in the canyon walls. The models allowed better visualization of the structure, including assessment of large-scale boudinage included in strain estimates reported here.

No evidence of the Harrisburg detachment fault was found in this study. Nonetheless, this conclusion is limited because in Surprise Canyon the expected position of the Harrisburg Detachment is occupied by a younger, brittle fault, Woodpecker fault. Thus, future work should focus along the strike of the Woodpecker fault where the structure does not cut out ductile structures at the level of the inferred Harrisburg Fault.

REFERENCES

Albee, A. L., Labotka, T. C., Lanphere, M. A., & McDowell, S. D. (1981). Geologic map of the Telescope Peak quadrangle. *California: US Geological Survey Geologic Quadrangle Map GQ-1532, Scale*, *1*(62,500), 1.

Allmendinger, R. W., Cardozo, N., & Fisher, D. M. (2011). *Structural geology algorithms: Vectors and tensors*. Cambridge University Press.

Andersson, U. B., Högdahl, K., Sjöström, H. akan, & Bergman, S. (2006). Multistage growth and reworking of the Palaeoproterozoic crust in the Bergslagen area, southern Sweden: evidence from U–Pb geochronology. *Geological Magazine*, *143*(5), 679–697.

Andrew, J. E. (2002). The Mesozoic and Tertiary tectonic history of the Panamint Range and Quail Mountains. *California [Ph. D. Thesis]: Lawrence, Kansas, University of Kansas*, 154.

Armin, R. A., & Mayer, L. (1983). Subsidence analysis of the Cordilleran miogeocline: Implications for timing of late Proterozoic rifting and amount of extension. *Geology*, *11*(12), 702–705.

Armstrong, R. L., & Suppe, J. (1973). Potassium-Argon Geochronometry of Mesozoic Igneous Rocks in Nevada, Utah, and Southern California. *Geological Society of America Bulletin*, *84*(4), 1375–1392. https://doi.org/10.1130/0016-7606(1973)84<1375:PGOMIR>2.0.CO;2

Barth, A. P., Wooden, J. L., Tosda, R. M., Morrison, J., Dawson, D. L., & Hernly, B. M. (1995). Origin of gneisses in the aureole of the San Gabriel anorthosite complex and implications for the Proterozoic crustal evolution of southern California. *Tectonics*, *14*(3), 736–752.

Brush, J. A., Pavlis, T. L., Hurtado, J. M., & Knott, J. R. (2015). *Evaluating methods of field-based 3D visualization and their application to mapping metamorphic terranes: An example from the Panamint Mountains, California*. The University of Texas at El Paso.

Burchfiel, B. C., Cowan, D. S., & Davis, G. A. (1992). Tectonic overview of the Cordilleran orogen. *The Cordilleran Orogen: Conterrninous US, The Geology of North America, G-3, Edited by BC Burchfiel, PW Lipman, and ML Zoback*, 407–479.

Busby-Spera, C. J., Martinson, J. M., Riggs, N. R., & Schermer, E. R. (1990). The Triassic-Jurassic magmatic arc in the Mojave-Sonoran deserts and the Sierran-Klamath region; similarities and differences in paleogeographic evolution. *Geological Society of America Special Papers*, *255*, 325–338.

Cardozo, N., & Allmendinger, R. W. (2013). Spherical projections with OSXStereonet. *Computers & Geosciences*, *51*, 193–205.

Chen, J. H., & Moore, J. G. (1979). Late Jurassic Independence dike swarm in eastern California. *Geology*, *7*(3), 129–133. https://doi.org/10.1130/0091-7613(1979)7<129:LJIDSI>2.0.CO;2

Cichanski, M. (2000). Low-angle, range-flank faults in the Panamint, Inyo, and Slate ranges, California: Implications for recent tectonics of the Death Valley region. *Geological Society of America Bulletin*, *112*(6), 871–883.

Cobb, J. A. (2015). *Understanding the contractional history of Surprise Canyon, California through digital field mapping, 3D modeling, and U-Pb zircon geochronology*. The University of Texas at El Paso.

Corsetti, F. A., & Kaufman, A. J. (2003). Stratigraphic investigations of carbon isotope anomalies and Neoproterozoic ice ages in Death Valley, California. *Geological Society of America Bulletin*, *115*(8), 916–932.

Corsetti, F. A., & Kaufman, A. J. (2005). The relationship between the Neoproterozoic Noonday Dolomite and the Ibex Formation: New observations and their bearing on 'snowball Earth.' *Earth-Science Reviews*, *73*(1–4), 63–78. https://doi.org/10.1016/j.earscirev.2005.07.002

DeCelles, P. G. (2004). Late Jurassic to Eocene evolution of the Cordilleran thrust belt and foreland basin system, western USA. *American Journal of Science*, *304*(2), 105–168.

Dehler, C. M., Elrick, M., Bloch, J. D., Crossey, L. J., Karlstrom, K. E., & Des Marais, D. J. (2005). High-resolution δ13C stratigraphy of the Chuar Group (ca. 770–742 Ma), Grand Canyon: Implications for mid-Neoproterozoic climate change. *Geological Society of America Bulletin*, *117*(1–2), 32–45.

Dehler, C. M., Elrick, M., Karlstrom, K. E., Smith, G. A., Crossey, L. J., & Timmons, J. M. (2001). Neoproterozoic Chuar Group (800–742Ma), Grand Canyon: a record of cyclic marine deposition during global cooling and supercontinent rifting. *Sedimentary Geology*, *141*, 465–499.

Dickinson, W. R. (2004). Evolution of the North American Cordillera. *Annual Review of Earth and Planetary Sciences*, *32*(1), 13–45. https://doi.org/10.1146/annurev.earth.32.101802.120257

Dunne, G. C., Garvey, T. P., Oborne, M., Schneidereit, D., Fritsche, A. E., & Walker, J. D. (1998). Geology of the Inyo Mountains Volcanic Complex: Implications for Jurassic paleogeography of the Sierran magmatic arc in eastern California. *Geological Society of America Bulletin*, *110*(11), 1376–1397. https://doi.org/10.1130/0016-7606(1998)110<1376:GOTIMV>2.3.CO;2

Evernden, J. F., & Kistler, R. W. (1970). *Chronology of emplacement of Mesozoic batholithic complexes in California and western Nevada*. Retrieved from https://pubs.er.usgs.gov/publication/pp623

Fairchild, I. J., & Kennedy, M. J. (2007). Neoproterozoic glaciation in the Earth System. *Journal of the Geological Society*, *164*(5), 895–921.

Fedo, C. M., & Cooper, J. D. (2001). Sedimentology and sequence stratigraphy of Neoproterozoic and Cambrian units across a craton-margin hinge zone, southeastern California, and implications for the early evolution of the Cordilleran margin. *Sedimentary Geology*, *141*, 501–522.

Gehrels, G. E., Valencia, V. A., & Ruiz, J. (2008). Enhanced precision, accuracy, efficiency, and spatial resolution of U-Pb ages by laser ablation–multicollector–inductively coupled plasma–mass spectrometry. *Geochemistry, Geophysics, Geosystems*, *9*(3).

Gehrels, G., & Pecha, M. (2014). Detrital zircon U-Pb geochronology and Hf isotope geochemistry of Paleozoic and Triassic passive margin strata of western North America. *Geosphere*, *10*(1), 49–65.

Greene, D. C., Stevens, C. H., & Wise, J. M. (1997). The Laurel-Convict fault, eastern Sierra Nevada, California: A Permo–Triassic left-lateral fault, not a Cretaceous intrabatholithic break. *Geological Society of America Bulletin*, *109*(4), 483–488. https://doi.org/10.1130/0016-7606(1997)109<0483:TLCFES>2.3.CO;2

Hammond, J. G. (1986). Geochemistry and petrogenesis of Proterozoic diabase in the southern Death Valley region of California. *Contributions to Mineralogy and Petrology*, *93*(3), 312–321.

Hammond, J. L. G. (1983). *Late Precambrian diabase intrusions in the southern Death Valley region, California: their petrology, geochemistry, and tectonic significance*. University of Southern California.

Harding, M. B. (1987). The geology of the Wildrose Peak Area, Panamint Mountains, California. *Masters Abstracts International*, *45*.

Hazzard, J. C. (1937). *Paleozoic section in the Nopah and Resting Springs Mountains, Inyo County, California*. California Journal of Mines and Geology.

Heaman, L. M., & Grotzinger, J. P. (1992). 1.08 Ga diabase sills in the Pahrump Group, California: Implications for development of the Cordilleran miogeocline. *Geology*, *20*(7), 637–640.

Hodges, K. V., McKenna, L. W., & Harding, M. B. (1990). Structural unroofing of the central Panamint Mountains, Death Valley region, southeastern California. *Geological Society of America Memoirs*, *176*, 377–390.

Hodges, K. V., Walker, J. D., & Wernicke, B. P. (1987). Footwall structural evolution of the Tucki Mountain detachment system, Death Valley region, southeastern California. *Geological Society, London, Special Publications*, *28*(1), 393–408. https://doi.org/10.1144/GSL.SP.1987.028.01.24

Hurtgen, M. T., Arthur, M. A., & Prave, A. R. (2004). The sulfur isotope composition of carbonate-associated sulfate in Mesoproterozoic to Neoproterozoic carbonates from Death Valley, California. *Geological Society of America Special Papers*, *379*, 177–194.

Johnson, B. K. (1957). Geology of a part of the Manly Peak quadrangle, southern Panamint Range, California. *University of California Publications in Geological Sciences, 30, pp. 353–424*.

Kupfer, D. H. (1960). Thrust Faulting and Chaos Structure, Silurian Hills, San Bernardino County, California. *Geological Society of America Bulletin*, *71*(2), 181–214. https://doi.org/10.1130/0016-7606(1960)71[181:TFACSS]2.0.CO;2

Labotka, Albee, A. L., Lanphere, M. A., & McDowell, S. D. (1980). Stratigraphy, Structure, and Metamorphism in the Central Panamint Mountains (Telescope Peak Quadrangle), Death Valley Area, California. *Geological Society of America Bulletin*, *91*(3_Part_II), 843–933. https://doi.org/10.1130/GSAB-P2-91-843

Labotka, T. C. (1981). Petrology of an andalusite-type regional metamorphic terrane, Panamint Mountains, California. *Journal of Petrology*, *22*(2), 261–296.

Labotka, Theodore Charles. (1978). *Geology of the Telescope Peak Quadrangle, California and late Mesozoic regional metamorphism, Death Valley area, California*. California Institute of Technology.

Lanphere, M. A., Wasserburg, G. J. F., Albee, A. L., & Tilton, G. R. (1964). *Redistribution of strontium and rubidium isotopes during metamorphism, World Beater Complex, Panamint Range, California*. Retrieved from http://resolver.caltech.edu/CaltechAUTHORS:20160125-145554089

Le Heron, D. P., Tofaif, S., Vandyk, T., & Ali, D. O. (2017). A diamictite dichotomy: Glacial conveyor belts and olistostromes in the Neoproterozoic of Death Valley, California, USA. *Geology*, *45*(1), 31–34. https://doi.org/10.1130/G38460.1

Macdonald, F. A., Prave, A. R., Petterson, R., Smith, E. F., Pruss, S. B., Oates, K., … Fallick, A. E. (2013). The Laurentian record of Neoproterozoic glaciation, tectonism, and eukaryotic evolution in Death Valley, California. *Geological Society of America Bulletin*, *125*(7–8), 1203–1223.

Macdonald, F. A., Schmitz, M. D., Crowley, J. L., Roots, C. F., Jones, D. S., Maloof, A. C., … Schrag, D. P. (2010). Calibrating the Cryogenian. *Science, 327*(5970), 1241–1243. https://doi.org/10.1126/science.1183325

Mahon, R. C., Dehler, C. M., Link, P. K., Karlstrom, K. E., & Gehrels, G. E. (2014). Geochronologic and stratigraphic constraints on the Mesoproterozoic and Neoproterozoic Pahrump Group, Death Valley, California: A record of the assembly, stability, and breakup of Rodinia. *Geological Society of America Bulletin*, *126*(5–6), 652–664.

Maud, R. L. (1979). *Stratigraphy and depositional environments of the carbonate-terrigenous member of the Crystal Spring Formation Death Valley, California* (M.S.). University Park, Pennsylvania State University.

Maud, R. L. (1983). *Stratigraphy, petrography and depositional environments of the carbonate-terrigenous member of the Crystal Spring Formation Death Valley, California* (PhD). State College, Pennsylvania, The Pennsylvania State University.

Mbuyi, K., & Prave, A. R. (1993). Unconformities in the mid-late Proterozoic Pahrump Group: stratigraphic evidence from the upper member Crystal Spring Formation. *Geological Society of America, Abstracts with Programs;(United States)*, *25*(CONF-9305259--).

McKenna, L. W., & Hodges, K. V. (1990). Constraints on the kinematics and timing of late Miocene-Recent extension between the Panamint and Black Mountains, southeastern California. *Geological Society of America Memoirs*, *176*, 363–376.

Miller, C. F. (1978). *An Early Mesozoic Alkalic Magmatic Belt in Western North America*. 163–173.

Miller, J. M. G. (1983). *Stratigraphy and sedimentology of the upper Proterozoic Kingston Peak Formation, Panamint Range, eastern California*. Retrieved from http://adsabs.harvard.edu/abs/1983PhDT.....22M

Miller, J. M. G., Troxel, B. W., & Wright, L. A. (1988). Stratigraphy and paleogeography of the Proterozoic Kingston Peak Formation, Death Valley region, eastern California. *South Coast Geological Society*.

Miller, Julia M. G. (1985). Glacial and syntectonic sedimentation: The upper Proterozoic Kingston Peak Formation, southern Panamint Range, eastern California. *Geological Society of America Bulletin*, *96*(12), 1537–1553. https://doi.org/10.1130/0016-7606(1985)96<1537:GASSTU>2.0.CO;2

Mrofka, D. D. (2010). *Competing models for the timing of Cryogenian Glaciation: Evidence from the Kingston Peak Formation, southeastern California*. Retrieved from https://escholarship.org/uc/item/3ph3f3ps.pdf

Mrofka, D., & Kennedy, M. (2011). The Kingston Peak Formation in the eastern Death Valley region. *Geological Society, London, Memoirs*, *36*(1), 449–458.

Norton, I. (2011). Two-stage formation of Death Valley. *Geosphere*, *7*(1), 171–182. https://doi.org/10.1130/GES00588.1

Pavlis, T. L., Brush, J. A., & Cobb, J. (2016). *MESOZOIC DUCTILE DEFORMATION IN THE PANAMINT MOUNTAINS: SEVIER CONTRACTION OVERPRINTED BY LARAMIDE AGE HINTERLAND-VERGENT FOLDING*. https://doi.org/10.1130/abs/2016CD-274269

Pavlis, T. L., Langford, R., Hurtado, J., & Serpa, L. (2010). Computer-based data acquisition and visualization systems in field geology: Results from 12 years of experimentation and future potential. *Geosphere*, *6*(3), 275–294.

Petterson, R., Prave, A. R., & Wernicke, B. P. (2011). Chapter 41 Glaciogenic and related strata of the Neoproterozoic Kingston Peak Formation in the Panamint Range, Death Valley region, California. *Geological Society, London, Memoirs*, *36*(1), 459–465. https://doi.org/10.1144/M36.41

Petterson, R., Prave, A. R., Wernicke, B. P., & Fallick, A. E. (2011). The Neoproterozoic Noonday Formation, Death Valley region, California. *Geological Society of America Bulletin*, *123*(7–8), 1317–1336.

Prave, A. R. (1994). The Pahrump Group: Alternative speculations on the Neoproterozoic geodynamic development of the Death Valley region. *Geological Society of America Abstracts with Programs*, *26*, 82.

Prave, A. R. (1999). Two diamictites, two cap carbonates, two δ13C excursions, two rifts: The Neoproterozoic Kingston Peak Formation, Death Valley, California. *Geology*, *27*(4), 339–342. https://doi.org/10.1130/0091-7613(1999)027<0339:TDTCCT>2.3.CO;2

Prave, Anthony R. (2000). Two diamictites, two cap carbonates, two δ13C excursions, two rifts: The Neoproterozoic Kingston Peak Formation, Death Valley, California: Comment and Reply, REPLY. *Geology*, *28*(2), 192–192.

Rämö, T. O., Calzia, J. P., & Kosunen, P. J. (2002). Geochemistry of Mesozoic plutons, southern Death Valley region, California: Insights into the origin of Cordilleran interior magmatism. *Contributions to Mineralogy and Petrology*, *143*(4), 416–437. https://doi.org/10.1007/s00410-002-0354-9

Roberts, M. T. (1976). Stratigraphy and depositional environments of the Crystal Spring Formation, southern Death Valley region, California. *Geologic Features—Death Valley, California: California Division of Mines and Geology Special Report 106*, 35–44.

Roberts, M. T. (1982). Depositional environments and tectonic setting of the Crystal Spring Formation, Death Valley region, California. *Geology of Selected Areas in the San Bernardino Mountains, Western Mojave Desert, and Southern Great Basin, California: Geological Society of America Cordilleran Section Field Trip Guidebook and Volume: Shoshone, California, Death Valley Publishing Company*, 143–154.

Rose, C. V., & Maloof, A. C. (2010). Testing models for post-glacial 'cap dolostone' deposition: Nuccaleena Formation, South Australia. *Earth and Planetary Science Letters*, *296*(3–4), 165–180. https://doi.org/10.1016/j.epsl.2010.03.031

Schweickert, R. A., & Lahren, M. M. (1987). Continuation of Antler and Sonoma orogenic belts to the eastern Sierra Nevada, California, and Late Triassic thrusting in a compressional arc. *Geology*, *15*(3), 270–273. https://doi.org/10.1130/0091-7613(1987)15<270:COAASO>2.0.CO;2

Serpa, L., & Pavlis, T. L. (1996). Three-dimensional model of the late Cenozoic history of the Death Valley region, southeastern California. *Tectonics*, *15*(6), 1113–1128.

Smith, E. F., MacDonald, F. A., Crowley, J. L., Hodgin, E. B., & Schrag, D. P. (2016). Tectonostratigraphic evolution of the c. 780–730 Ma Beck Spring Dolomite: Basin Formation in the core of Rodinia. *Geological Society, London, Special Publications*, *424*(1), 213–239. https://doi.org/10.1144/SP424.6

Speed, R. C., & Lintz Jr, J. (1984). Paleozoic and Mesozoic continental margin collision zone features. *Western Geological Excursions: Reno, Nevada, University of Nevada, Geological Society of America Annual Meeting Field Trip Guidebook*, *4*, 66–80.

Stevens, C. H. (1986). Evolution of the Ordovician through Middle Pennsylvanian carbonate shelf in east-central California. *Geological Society of America Bulletin*, *97*(1), 11–25.

Stevens, C. H., Stone, P., Dunne, G. C., Greene, D. C., Walker, J. D., & Swanson, B. J. (1997). Paleozoic and Mesozoic Evolution of East-Central California. *International Geology Review*, *39*(9), 788–829. https://doi.org/10.1080/00206819709465303

Stewart, J. H. (1970). Upper Precambrian and Lower Cambrian strata in the southern Great Basin, California and Nevada: USGS Professional Paper 620. *US Geological Survey, Reston*.

Stewart, J. H., & Poole, F. G. (1974). *Lower Paleozoic and uppermost Precambrian Cordilleran miogeocline, Great Basin, western United States*.

Strickland, A., Wooden, J. L., Mattinson, C. G., Ushikubo, T., Miller, D. M., & Valley, J. W. (2013). Proterozoic evolution of the Mojave crustal province as preserved in the Ivanpah Mountains, southeastern California. *Precambrian Research*, *224*, 222–241.

Timmons, J. M., Karlstrom, K. E., Dehler, C. M., Geissman, J. W., & Heizler, M. T. (2001). Proterozoic multistage (ca. 1.1 and 0.8 Ga) extension recorded in the Grand Canyon Supergroup and establishment of northwest-and north-trending tectonic grains in the southwestern United States. *Geological Society of America Bulletin*, *113*(2), 163–181.

Timmons, J. M., Karlstrom, K. E., Heizler, M. T., Bowring, S. A., Gehrels, G. E., & Crossey, L. J. (2005). Tectonic inferences from the ca. 1255–1100 Ma Unkar Group and Nankoweap Formation, Grand Canyon: Intracratonic deformation and basin formation during protracted Grenville orogenesis. *Geological Society of America Bulletin*, *117*(11–12), 1573–1595.

Troxel, B. W. (1966). Sedimentary Features of the Later Precambrian Kingston Peak Formation Death Valley, California. *Geological Society of America Special Paper*, *101*, 341.

Troxel, Bennie W. (1967). Sedimentary rocks of late Precambrian and Cambrian age in the southern Salt Spring Hills, southeastern Death Valley, California. *California Division of Mines and Geology Special Report 92*, 33–41.

Tucker, M. E. (1986). Formerly aragonitic limestones associated with tillites in the late Proterozoic of Death Valley, California. *Journal of Sedimentary Research, 56*(6). Retrieved from http://archives.datapages.com/data/doi/10.1306/212F8A5D-2B24-11D7-8648000102C1865D

Walker, J. D., Burchfiel, B. C., & Davis, G. A. (1995). New age controls on initiation and timing of foreland belt thrusting in the Clark Mountains, southern California. *GSA Bulletin, 107*(6), 742–750. https://doi.org/10.1130/0016-7606(1995)107<0742:NACOIA>2.3.CO;2

Wasserberg, G. J., Wetherill, G. W., & Wright, L. A. (1959). Ages in the Precambrian terrane of Death Valley, California. *The Journal of Geology*, 702–708.

Wright, L. A. (1954). Geology of the Alexander Hills area, Inyo and San Bernardino Counties, Map Sheet 17. *Geology of Southern California, California Department of Natural Resources, Division of Mines Bulletin, 170*.

Wright, L. A., & Troxel, B. W. (1967). Limitations on right-lateral, strike-slip displacement, Death Valley and Furnace Creek fault zones, California. *Geological Society of America Bulletin, 78*(8), 933–950.

Wright, L. A., & Troxel, B. W. (1968). *Talc deposits of the southern Death Valley-Kingston Range region, California*. California Division of Mines and Geology.

Wright, L. A., Troxel, B. W., & Prave, A. R. (1992). Field traverse of Proterozoic rock units, Alexander Hills and southern Nopah Range, Death Valley region, CA. *Geological Society*

of America Penrose Conference: Late Precambrian Plate Tectonics and the Dawn of the Phanerozoic. Geological Society of America, Boulder, CO, 1–11.

Wright, L. A., Troxel, B. W., Williams, E. G., Roberts, M. T., & Diehl, P. E. (1976). Precambrian sedimentary environments of the Death Valley region, eastern California. *Geologic Features, Death Valley, California, Special Report*, *106*, 7–15.

APPENDIX

Table 1. Stable Isotope Data of Carbonates

Sample	Stratigraphic position in meters	$\delta^{13}C$ ‰ (VPDB)	Geologic Unit
6sc16	25	0.00	BS Marble
8sc16	13	3.46	BS Marble
9sc16	169	2.99	BS Marble
2sc16	1	3.38	BS Marble
10sc16	13	2.82	BS Marble
13sc16	106	4.04	BS Dolomite
14sc16	395	2.21	BS Dolomite
15sc16	388	2.22	BS Dolomite
16sc16	363	0.98	BS Dolomite
4SP16	1	2.00	BS Dolomite
1sc16	-19.9	3.38	HTS Marble
3sc16	-1	0.28	HTS Marble
4sc16	-2.2	1.95	HTS Marble
5sc16	-19.9	2.38	HTS Marble
5SP16	-1	1.95	HTS Formation
2sp16	-50	2.66	HTS Formation
6SP16	-25	-1.40	HTS Formation
7SP16	-40	-1.75	HTS Formation
1SP16	-120	-2.52	CS Marble
14dp41	*	1.440	BS Marble
14dp42	*	2.747	BS Marble
14dp43a	*	-0.581	CS Marble
11sc16	*	2.257	BS Marble
12sc16	*	2.044	BS Marble
16dp01	*	-0.343	Noonday Marble

Table 2. SPD18 U-Pb Data

						Isotope ratios						Apparent ages (Ma)								
grain #	Analysis	U	206Pb	U/Th	206Pb*	±	207Pb*	±	206Pb*	±	error	206Pb*	±	207Pb*	±	206Pb*	±	best age	±	Conc
	SPD18	(ppm)	204Pb		207Pb*	(%)	235U*	(%)	238U	(%)	corr.	238U*	(Ma)	235U	Ma)	207Pb*	(Ma)	(Ma)	(Ma)	(%)
1	Spot 36	475	17710	1.3	20.0195	1.3	0.1893	2.4	0.0275	2.0	0.84	174.9	3.5	176.0	3.9	192.8	30.2	174.9	3.5	1.01
	Spot 37	1897	39485	12.3	20.3230	1.2	0.1856	2.4	0.0274	2.1	0.86	174.0	3.6	172.8	3.8	157.6	28.3	174.0	3.6	0.99
	Spot 38	5907	433646	0.9	19.7084	1.0	0.1934	2.3	0.0277	2.1	0.90	175.9	3.6	179.5	3.8	229.0	23.5	175.9	3.6	1.02
2	Spot 39	520	27146	1.4	20.0980	1.2	0.1906	3.8	0.0278	3.6	0.95	176.8	6.3	177.2	6.2	183.6	26.9	176.8	6.3	1.00
	Spot 40	4840	56744	0.7	20.1469	0.9	0.1940	2.6	0.0284	2.4	0.94	180.3	4.3	180.0	4.3	177.9	20.5	180.3	4.3	1.00
3	Spot 41	406	16617	1.9	20.0217	1.5	0.1973	2.8	0.0287	2.3	0.84	182.2	4.2	182.8	4.6	192.5	34.9	182.2	4.2	1.00
	Spot 42	953	293037	1.6	19.6496	1.6	0.2008	3.3	0.0286	2.9	0.88	181.9	5.2	185.8	5.6	235.9	36.2	181.9	5.2	1.02
4	Spot 43	665	33002	0.8	19.9660	1.5	0.1905	3.5	0.0276	3.2	0.91	175.5	5.6	177.0	5.7	198.9	34.4	175.5	5.6	1.01
	Spot 44	5907	188561	0.6	20.0380	1.2	0.1990	3.1	0.0289	2.9	0.92	183.8	5.2	184.2	5.3	190.6	27.8	183.8	5.2	1.00
5	Spot 45	2569	50276	1.3	19.9527	1.5	0.1976	3.0	0.0286	2.6	0.87	181.8	4.6	183.1	5.0	200.5	34.5	181.8	4.6	1.01
	Spot 46	865	13217	1.6	20.3451	1.5	0.1901	3.5	0.0281	3.2	0.91	178.4	5.7	176.7	5.8	155.1	34.8	178.4	5.7	0.99
6	Spot 47	4126	58853	1.1	19.8877	0.7	0.2001	2.4	0.0289	2.3	0.95	183.5	4.1	185.2	4.0	208.0	16.4	183.5	4.1	1.01
	Spot 48	791	21122	1.3	20.2471	1.3	0.1874	4.0	0.0275	3.8	0.95	175.1	6.5	174.4	6.4	166.4	30.2	175.1	6.5	1.00
7	Spot 49	4157	69801	1.7	19.9780	1.4	0.1922	2.8	0.0279	2.5	0.87	177.2	4.3	178.5	4.7	197.6	32.9	177.2	4.3	1.01
	Spot 50	804	14134	1.0	20.2458	1.0	0.1838	2.8	0.0270	2.6	0.93	171.7	4.4	171.3	4.4	166.5	24.0	171.7	4.4	1.00
8	Spot 51	1520	76937	1.5	19.8734	1.2	0.1920	2.8	0.0277	2.5	0.91	176.1	4.4	178.4	4.6	209.7	26.8	176.1	4.4	1.01
9	Spot 52	1691	60654	1.3	19.6361	2.0	0.2090	4.1	0.0298	3.6	0.88	189.2	6.7	192.7	7.2	237.5	45.8	189.2	6.7	1.02
	Spot 53	366	7780	1.3	20.2350	1.5	0.1855	3.3	0.0272	3.0	0.90	173.2	5.1	172.8	5.3	167.7	34.7	173.2	5.1	1.00
10	Spot 54	5907	348685	1.3	19.9523	1.1	0.1979	2.9	0.0286	2.7	0.92	182.1	4.8	183.3	4.9	200.6	26.6	182.1	4.8	1.01
	Spot 55	1517	30375	1.6	19.5928	1.1	0.1987	3.3	0.0282	3.1	0.94	179.6	5.6	184.0	5.6	242.6	25.2	179.6	5.6	1.02
11	Spot 56	1011	30583	1.8	19.8365	1.5	0.1914	2.7	0.0275	2.3	0.83	175.1	3.9	177.8	4.5	214.1	35.3	175.1	3.9	1.02
12	Spot 57	5907	160187	1.2	19.6715	1.2	0.1977	2.9	0.0282	2.7	0.92	179.4	4.8	183.2	4.9	233.4	26.8	179.4	4.8	1.02
13	Spot 58	357	50090	1.9	19.6223	1.4	0.2001	3.1	0.0285	2.8	0.89	181.1	5.0	185.2	5.3	239.1	32.9	181.1	5.0	1.02
	Spot 59	5907	377625	0.9	19.7753	1.0	0.1990	3.4	0.0286	3.3	0.95	181.5	5.8	184.3	5.8	221.2	24.2	181.5	5.8	1.02
14	Spot 60	5311	376068	0.9	20.0280	1.0	0.1997	2.6	0.0290	2.4	0.93	184.4	4.3	184.9	4.3	191.8	22.6	184.4	4.3	1.00
	Spot 61	1664	37492	1.3	19.5503	1.8	0.1918	3.9	0.0272	3.4	0.89	173.0	5.8	178.1	6.3	247.6	41.2	173.0	5.8	1.03
15	Spot 62	3986	179339	0.9	20.0283	1.3	0.2010	2.7	0.0292	2.3	0.88	185.6	4.3	186.0	4.6	191.7	30.0	185.6	4.3	1.00
16	Spot 63	5907	246584	0.5	20.0886	1.4	0.1912	2.5	0.0279	2.1	0.83	177.2	3.6	177.7	4.1	184.7	32.1	177.2	3.6	1.00
17	Spot 64	919	16488	1.3	20.1602	1.5	0.1909	3.0	0.0279	2.6	0.86	177.5	4.5	177.4	4.9	176.4	35.3	177.5	4.5	1.00
18	Spot 65	617	74213	1.2	19.5696	1.6	0.2023	3.8	0.0287	3.5	0.91	182.6	6.3	187.1	6.5	245.3	36.3	182.6	6.3	1.02
	Spot 66	5907	49988	1.5	19.7173	0.8	0.1880	2.8	0.0269	2.7	0.96	171.1	4.6	175.0	4.5	228.0	17.7	171.1	4.6	1.02
19	Spot 67	1422	124362	1.4	19.7416	1.2	0.1939	3.0	0.0278	2.7	0.92	176.6	4.7	180.0	4.9	225.1	27.3	176.6	4.7	1.02
20	Spot 68	5907	212385	0.5	19.8711	1.0	0.1892	4.3	0.0273	4.1	0.97	173.5	7.1	176.0	6.9	210.0	24.3	173.5	7.1	1.01
19	Spot 69	399	102988	1.5	19.2497	1.6	0.2050	3.8	0.0286	3.4	0.91	182.0	6.1	189.4	6.5	283.2	36.3	182.0	6.1	1.04
21	Spot 70	396	28240	1.7	19.9892	1.8	0.2067	4.4	0.0300	4.0	0.91	190.4	7.6	190.8	7.7	196.3	42.4	190.4	7.6	1.00

Table 3. SPD18 Hafnium Data

grain	Analysis	(^{176}Yb + ^{176}Lu)/^{176}Hf (%)	Volts Hf	^{176}Hf/^{177}Hf	± (1s)	^{176}Lu/^{177}Hf	^{176}Hf/^{177}Hf (T)	**E-Hf (0)	E-Hf (0) ± (1s)	E-Hf (T)	Age (Ma)
2	Spot 39	17.6	3.8	0.28221	0.000020	0.0011	0.28220	-20.5	0.7	-16.7	177
	Spot 40	46.1	5.0	0.28229	0.000020	0.0029	0.28228	-17.5	0.7	-13.8	180
4	Spot 43	33.9	3.4	0.28210	0.000019	0.0021	0.28209	-24.2	0.7	-20.6	176
	Spot 44	44.1	7.5	0.28220	0.000017	0.0027	0.28219	-20.5	0.6	-16.8	184
5	Spot 46	32.8	3.6	0.28218	0.000019	0.0019	0.28217	-21.5	0.7	-17.7	178
7	Spot 49	50.6	5.4	0.28223	0.000025	0.0028	0.28222	-19.7	0.9	-16.0	182
	Spot 50	31.4	3.5	0.28213	0.000021	0.0020	0.28212	-23.2	0.7	-19.7	172
8	Spot 51	29.8	3.8	0.28222	0.000023	0.0017	0.28221	-20.1	0.8	-16.4	176
9	Spot 52	42.1	4.1	0.28214	0.000019	0.0025	0.28214	-22.6	0.7	-18.8	189
	Spot 53	17.9	3.4	0.28227	0.000023	0.0011	0.28227	-18.2	0.8	-14.5	173
10	Spot 54	55.1	7.1	0.28217	0.000020	0.0031	0.28216	-21.9	0.7	-18.2	182
	Spot 55	40.1	3.9	0.28225	0.000022	0.0024	0.28225	-18.7	0.8	-15.1	177
11	Spot 56	31.3	3.8	0.28224	0.000025	0.0020	0.28223	-19.4	0.9	-15.8	175
12	Spot 57	53.1	7.3	0.28220	0.000015	0.0032	0.28219	-20.8	0.5	-17.2	179
13	Spot 58	40.2	6.8	0.28222	0.000019	0.0023	0.28222	-19.8	0.7	-16.1	181
	Spot 59	22.7	3.7	0.28220	0.000024	0.0015	0.28219	-20.8	0.8	-16.9	182
14	Spot 60	59.8	4.8	0.28220	0.000025	0.0034	0.28219	-20.7	0.9	-17.0	184
	Spot 61	37.4	3.7	0.28220	0.000022	0.0022	0.28220	-20.6	0.8	-17.0	173
16	Spot 63	33.7	5.1	0.28216	0.000019	0.0020	0.28216	-22.0	0.7	-18.3	177
17	Spot 64	27.9	3.7	0.28219	0.000022	0.0016	0.28219	-20.9	0.8	-17.2	178
18	Spot 65	31.7	3.3	0.28229	0.000026	0.0020	0.28228	-17.6	0.9	-13.7	183
	Spot 66	34.3	9.3	0.28224	0.000017	0.0023	0.28223	-19.3	0.6	-15.8	171

Table 4. Strain Measurements Collected From Wildrose Canyon.

The long and short axes of stretched pebbles within the Wildrose Diamictite Member of the WKPF were measured along the foliation plane, and the surface perpendicular to lineation.

surface parallel to foliation (X/Y)				
Long axis	short axis	Elipticity $R_{X/Y} = l_a/s_a$	phi	ϕ in degrees
11	10	1.1	0.8	47.7
21	6	3.5	1.3	74.1
9	5	1.8	1.1	60.9
10	6	1.7	1.0	59.0
58	15	3.9	1.3	75.5
32	6	5.3	1.4	79.4
42	24	1.8	1.1	60.3
35	15	2.3	1.2	66.8
32	16	2.0	1.1	63.4
15	11	1.4	0.9	53.7
9	7	1.3	0.9	52.1
14	6	2.3	1.2	66.8
12	3	4.0	1.3	76.0
20	10	2.0	1.1	63.4
15	10	1.5	1.0	56.3
36	20	1.8	1.1	60.9
27	20	1.4	0.9	53.5
11	4	2.8	1.2	70.0
28	12	2.3	1.2	66.8
15	10	1.5	1.0	56.3
62	29	2.1	1.1	64.9
10	10	1.0	0.8	45.0
24	9	2.7	1.2	69.4
18	7	2.6	1.2	68.7
98	42	2.3	1.2	66.8
Rx/y μ_H		1.9		

surface perpendicular to lineation (Y/Z)				
Long axis	short axis	Elipticity $R_{Y/Z} = l_a/s_a$	phi	ϕ in degrees
72	25	2.9	1.24	70.85
61	36	1.7	1.04	59.45
21	7	3.0	1.25	71.57
14	6	2.3	1.17	66.80
7	3	2.3	1.17	66.80
10	3	3.3	1.28	73.30
27	9	3.0	1.25	71.57
16	12	1.3	0.93	53.13
15	6	2.5	1.19	68.20
25	11	2.3	1.16	66.25
63	41	1.5	0.99	56.94
22	17	1.3	0.91	52.31
110	53	2.1	1.12	64.27
7	6	1.2	0.86	49.40
12	6	2.0	1.11	63.43
15	6	2.5	1.19	68.20
7	3	2.3	1.17	66.80
19	7	2.7	1.22	69.78
12	4	3.0	1.25	71.57
12	3	4.0	1.33	75.96
12	6	2.0	1.11	63.43
25	14	1.8	1.06	60.75
19	3	6.3	1.41	81.03
15	4	3.8	1.31	75.07
37	15	2.5	1.19	67.93
16	9	1.8	1.06	60.64
12	6	2.0	1.11	63.43
62	12	5.2	1.38	79.05
45	7	6.4	1.42	81.16
32	14	2.3	1.16	66.37
60	35	1.7	1.04	59.74
Ry/z μ_H		2.3		
max elipticity		4.3		

Table 5. Stretch Measurements Of Boudinage Collected From Surprise And Wildrose Canyons. In both canyons, measurements were taken perpendicular to the extension lineations

Figure	Lf	Li	Stretch = Lf/Li
Surprise canyon marble mass north wall model			
		22	
		21.5	
		38	
	174	81.5	2.1
Schematic of choclate boudinage in sourdough marble			
$Lext_{NW}$		10	
		20	
		8	
	84	38	2.2
$Lext_{NE}$		10	
		11	
		8	
		5	
	133	34	3.9
Sourdough			
1		1.3	
		3.08	
		2.7	
		3.6	
	19.46	10.68	1.8
2		1.15	
		1.2	
		1.47	
		1.8	
		1.2	
		3.6	
		4.1	
	23.06	14.52	1.6
3		6	
		1.76	
		2	
		2.1	
		1.7	
	22.5	13.56	1.7

Figure	Lf	Li	Stretch = Lf/Li
DSC03279			
1		5.6	
		9.3	
		2.17	
		1.3	
		0.8	
		6.75	
	45.3	25.92	1.7
		5.2	
2		4.1	
		11.9	
		5.25	
	33.5	26.45	1.3
DSC03245			
1		0.95	
		0.16	
		0.5	
		0.6	
		1.4	
		3.8	
		1.3	
		1.9	
		0.75	
	26	11.36	2.3
2		1.8	
		1.14	
		0.2	
		1.6	
		2.2	
		1.75	
		0.8	
3	22.8	9.49	2.4
		7.4	
		1.8	
		1.3	
		1.4	
		3	
		2.7	
	24.2	17.6	1.375

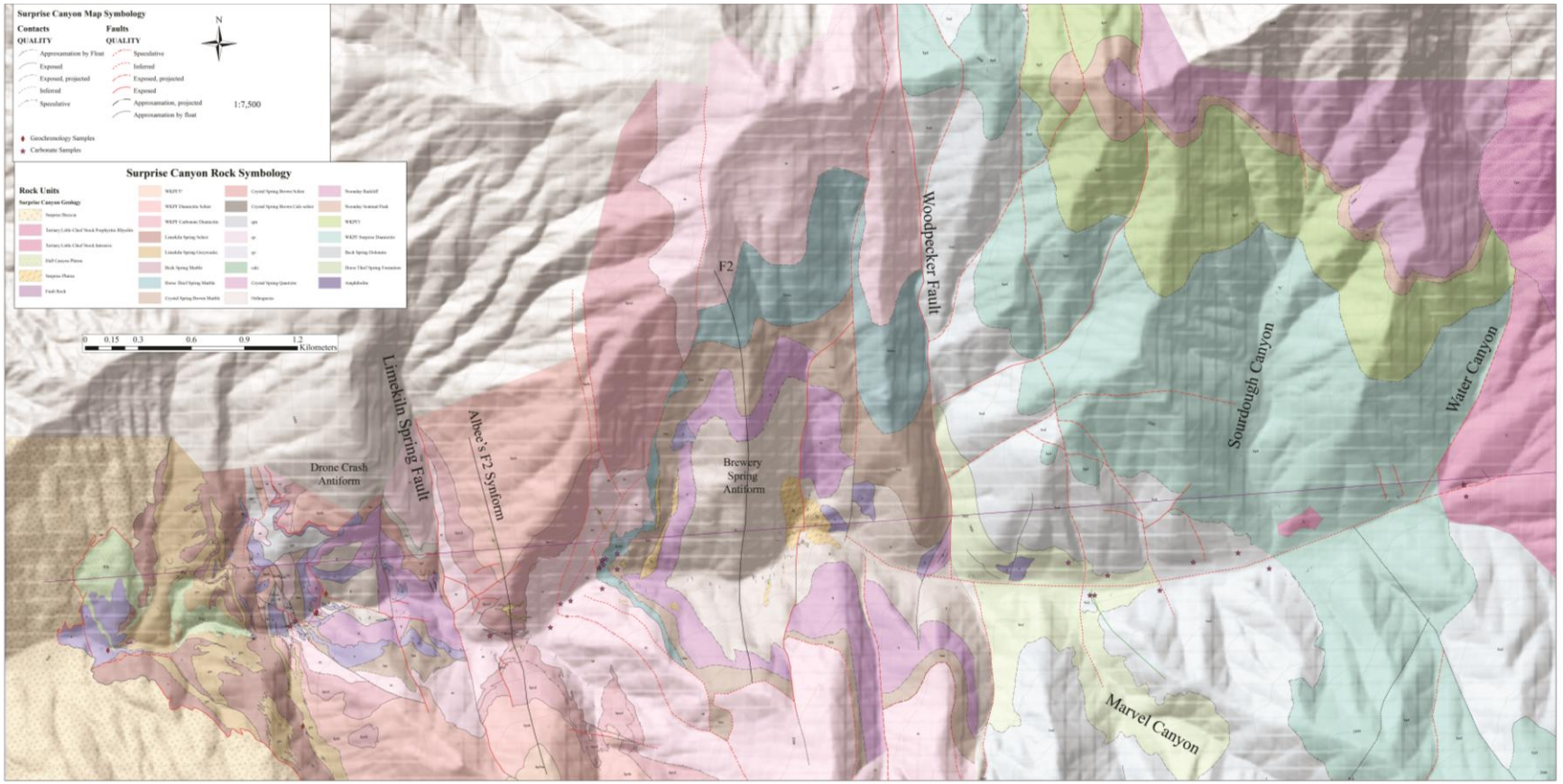

Plate 1. Geologic Map of Surprise Canyon

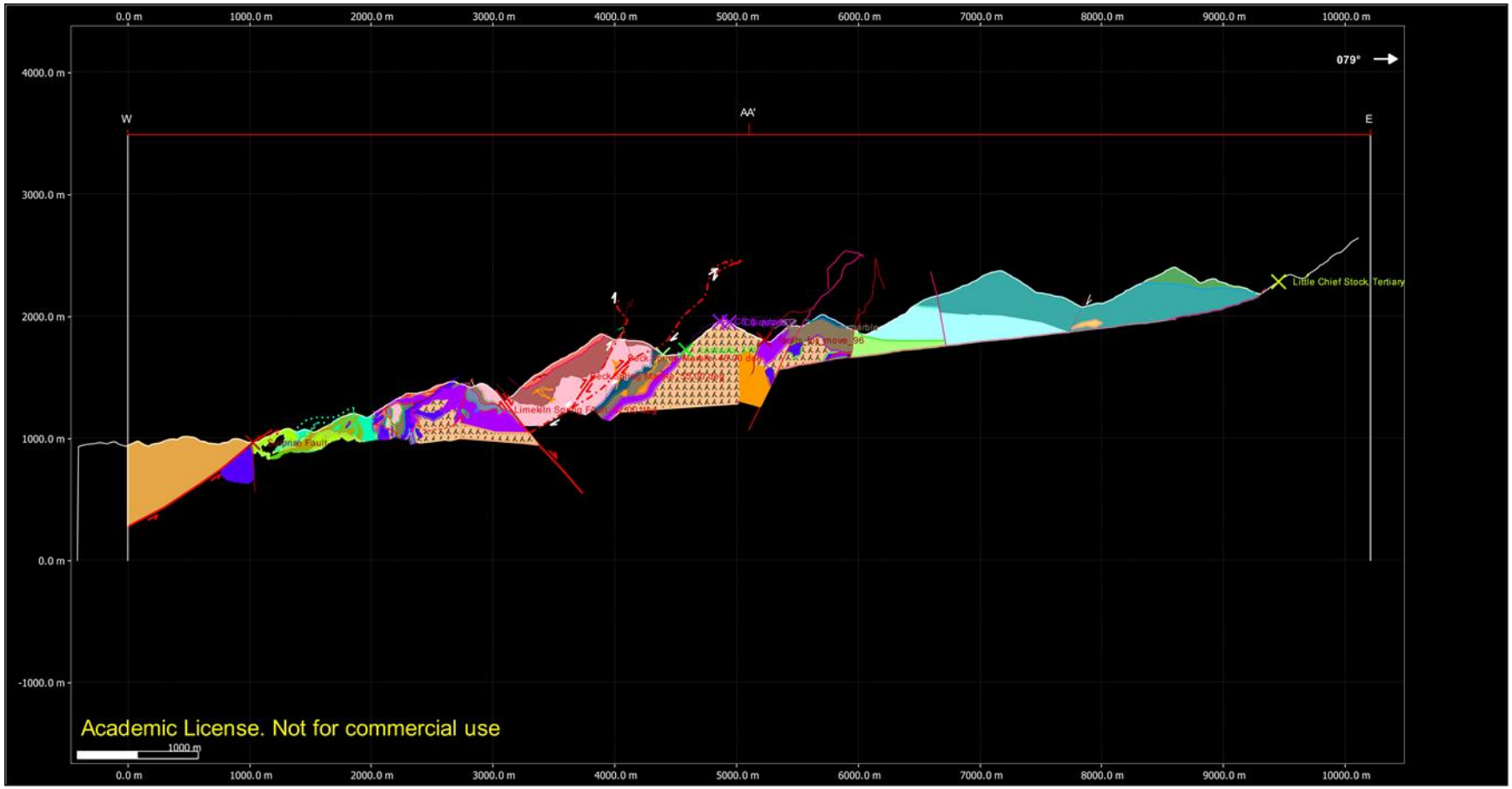

Plate 2. Surprise Canyon Cross Section AA’

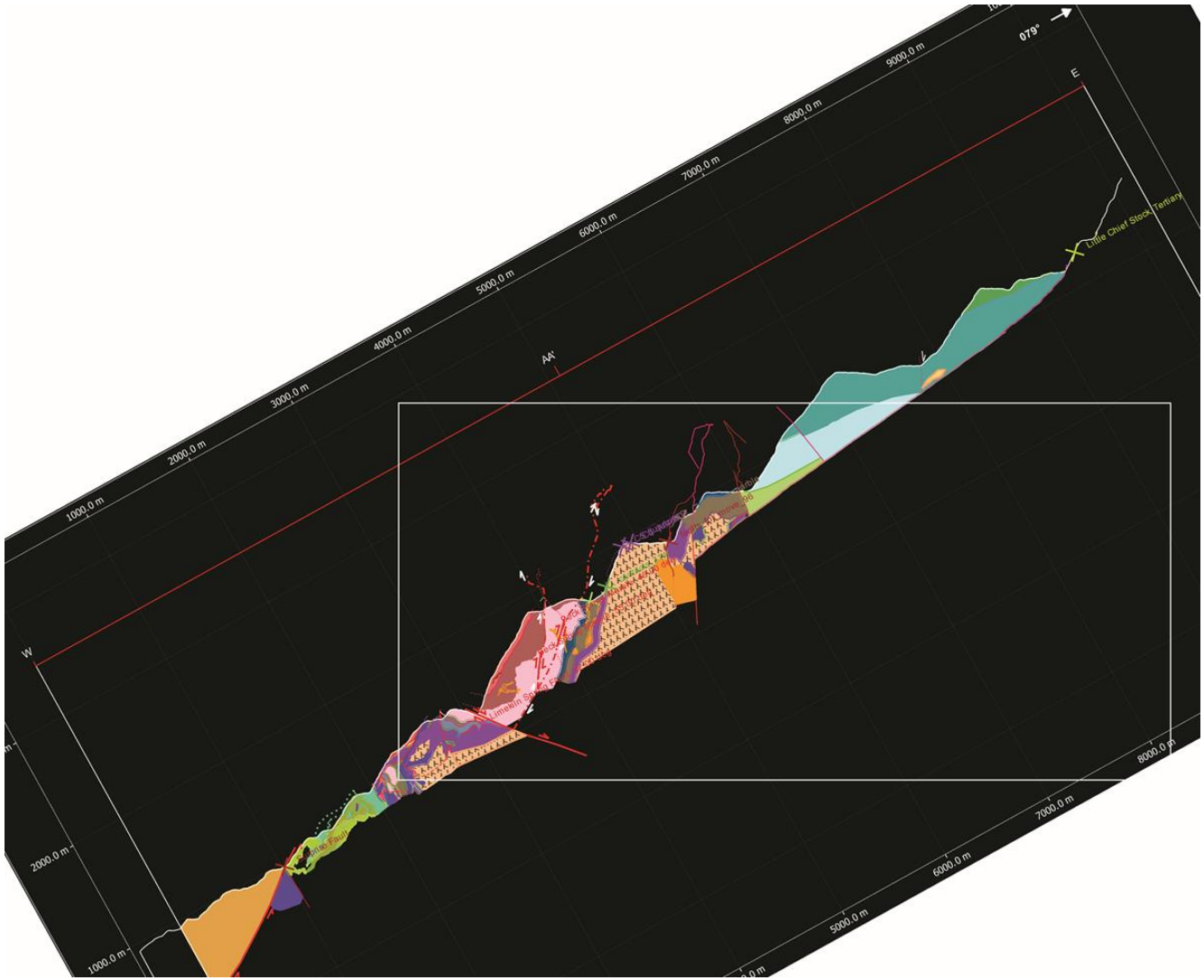

Plate 2b. Rotated Surprise Canyon Cross Section AA’

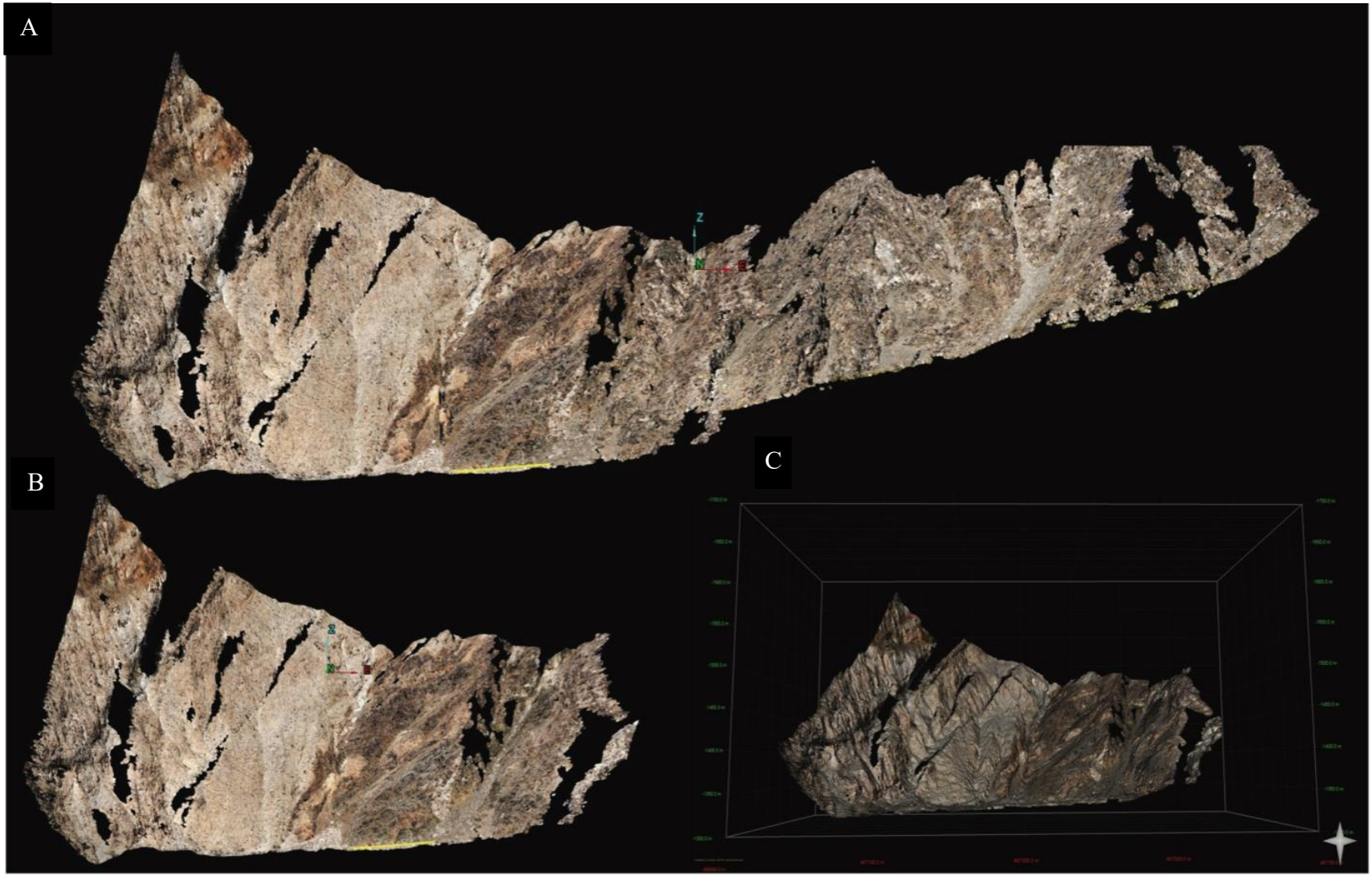

Plate 3. Photogrammetry Models

A. Combined photogrammetry models of the Pahrump Group intruded by the Surprise Pluton, and Orthogneiss located between Limekiln Spring and Brewery Spring, as viewed in Maptek, the perspective is due north. B. The Lower Pahrump Group model as viewed in Maptek, the perspective is due north. C. The Lower Pahrump Group model as viewed in Midland Valley Move, the perspective is due north. D. The orthogneiss model as viewed in Maptek, the perspective is due north, approximate orientation was achieved by freehand rotation.

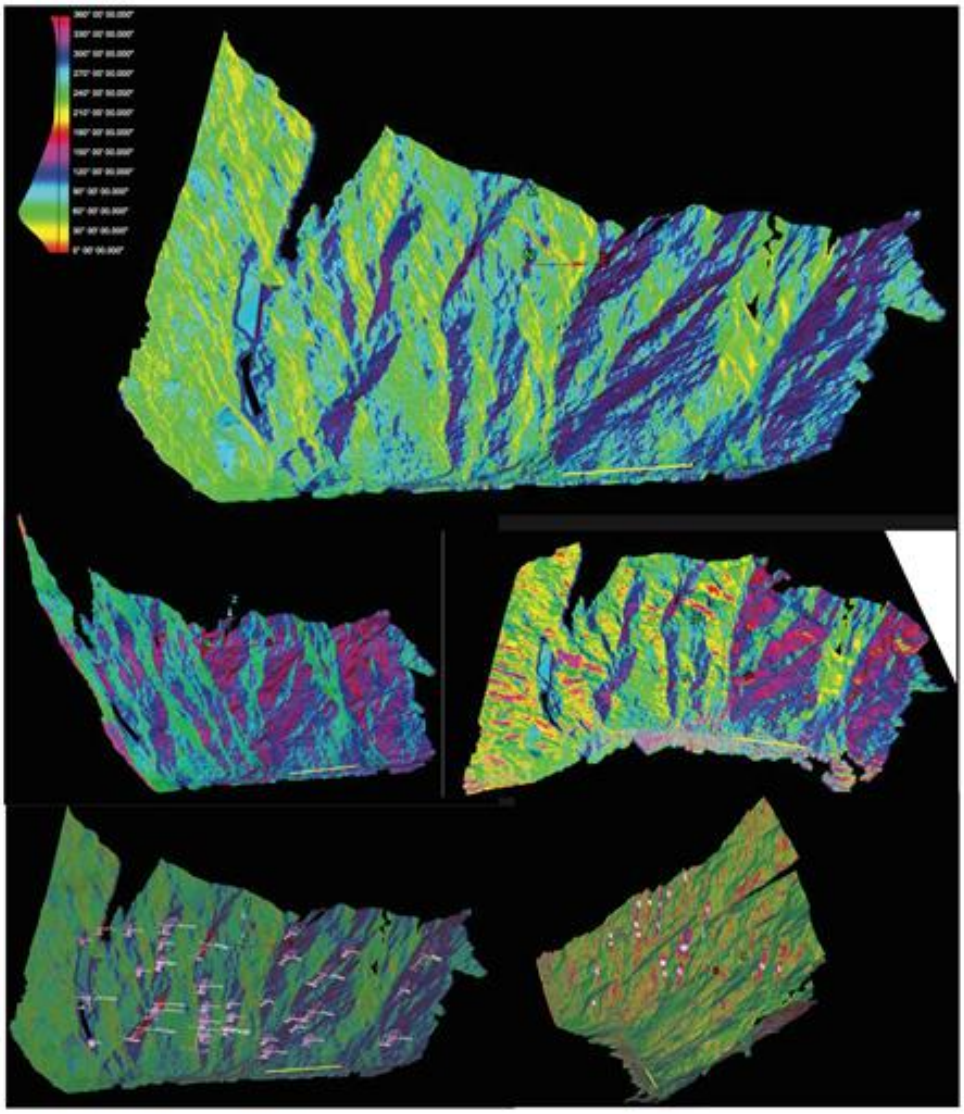

Plate 4. Color by Strike Derivation on Maptek Model

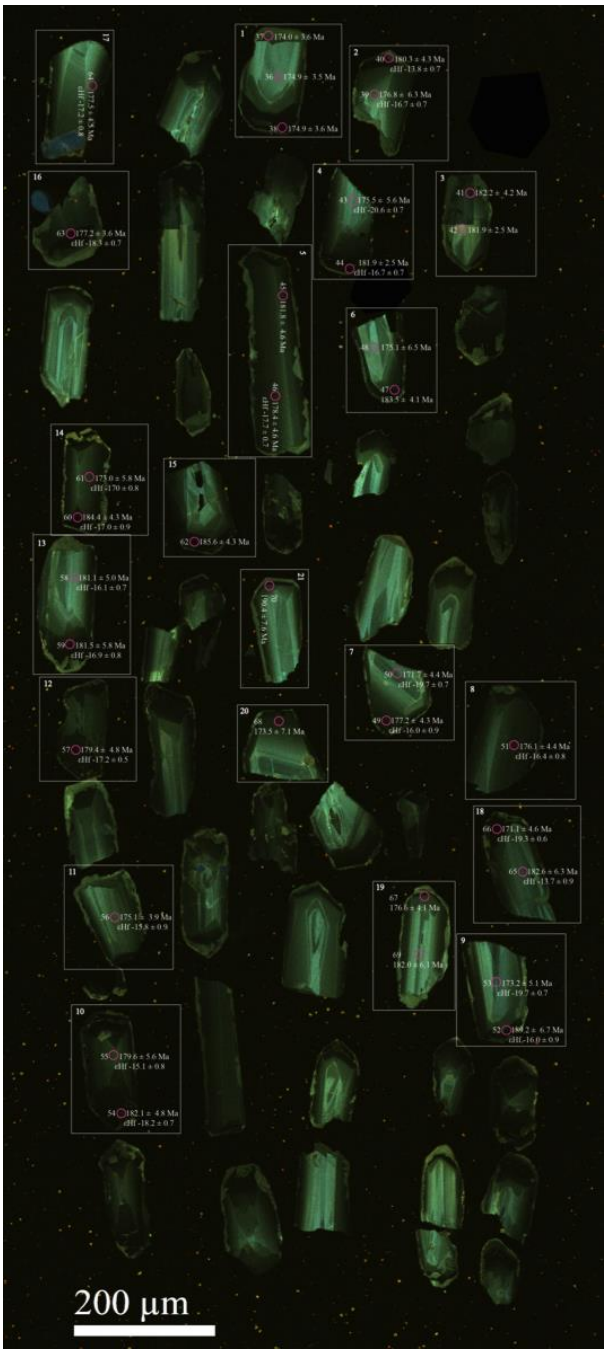

Plate 5. Cl Image of SPD18 Zircon Grains

Cathodoluminescence image of zircon grains collected from sample SPD18. The individual grains are labeled with spot analyses numbers and the corresponding $^{206}Pb/^{238}U$ Best Ages (Ma), and the epsilon of hafnium data if collected.

GLOSSARY

1. Argillite – A fine-grained sedimentary rock composed predominantly of hardened clay particles. Argillaceous rocks are basically lithified muds and oozes. Argillaceous rocks grade into shales when they develop the characteristic fissile layering.
2. Boudinage – A sausage shaped structure commonly found in strongly deformed sedimentary and metamorphic rocks, in which an original continuous competent layer or bed between less competent layers have been stretched, thinned, and broken at regular intervals into bodies resembling boudins or sausages, elongated parallel to the fold axes.
3. Concordia- comparison of $^{206}Pb/^{238}U$ ratio to $^{207}Pb/^{235}U$ ratio, strong concordia indicates a closed system (one interpretation) (Schoen 2014)
4. Diamictite – lithified, poorly sorted to non-sorted, land derived sediments associated with glacial events
5. Fabric – as related to metamorphic rocks, fabric describes the spatial and geometric configuration of all the elements that make it up. This provides information on both the orientation and magnitude of the strains that have affected a particular piece of deformed rock.
6. Facies
    a. Sedimentary facies – adjacent packages of sediment bearing different physical, chemical, and biological features with varying lateral thicknesses indicative of depositional environments over geologic time.
    b. Metamorphic facies – pressure and temperature conditions that result in specific mineral assemblages. The range of mineral assemblages in this study is ~1.5

kilobars to ~3 kilobars and 400° C to 600° C, denoted by the yellow box in the Pressure - Temperature diagram below.

i. Amphibolite facies conditions, grey area - ~2 kilobars to 14 kilobars, and ~540° C to ~750° C

ii. Greenschist facies conditions, green area - ~2 kilobars to ~10 kilobars, and ~325° C to ~540° C

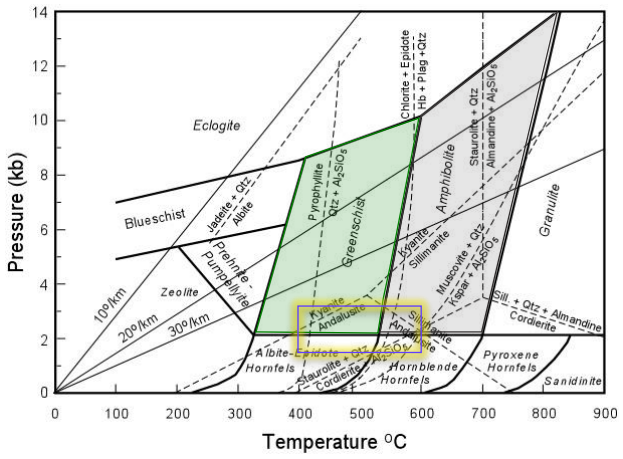

7. Metamorphic core complexes –

a. Coney (1980) stated that metamorphic core complexes are characterized by a generally heterogeneous, older metamorphic-plutonic basement terrane overprinted by low-dipping lineated and foliated mylonitic and gneissic fabrics. An unmetamorphosed cover terrane is typically attenuated and sliced by numerous sub horizontal younger-on-older faults. Between the basement and cover terranes is a decollement and/or steep metamorphic gradient with much brecciation and kinematic structural relationships indicating sliding or detachment. The decollement is also called a detachment fault.

b. Lister & Davis (1989) stated that metamorphic core complexes form as the result of major continental extension, when the middle and lower continental crust is dragged out from beneath the fracturing, extending upper crust. Movement zones capable of producing such effects evolve in space as well as with time. Deforming rocks in the footwall are uplifted through a progression of different metamorphic and deformational environments, producing a characteristic sequence of overprinted meso- and microstructures.

8. Miogeocline - Passive margin sediments, clastics (sands and conglomerates) that form a wedge and fan out basin-ward into finer particles like silts and clays, if there is a high stand (when water gets deep enough that carbonate precipitation occurs quickly) carbonate deposition also occurs in the deeper part of the basin where it precipitates out of solution.
9. Olistolith- megaclast in an olistrosome, can be one cubic kilometer in volume
10. Olistrosome – heterogenous matrix of sand and clay particles bearing megaclasts of carbonate and siliciclastic pre-glacial strata (Le Heron, Tofaif, Vandyk, & Ali, 2017)
11. Oncolite – grain composed of irregular concentric layers of algal/foraminiferal assemblages surrounding marine nuclei
12. Stratigraphy - the order and relative position of rock units (strata) and their relationship to the geological time scale.
    a. Chemostratigraphy - the technique of sediment characterization and correlation using subtle variations in the light stable isotope composition of the sediments.

13. Tholeiitic pillow basalts - Lavas are comprised alkaline mafic minerals: Calcium-rich plagioclases, augite, pigeonite or hypersthene, and maybe some olivine. The fluffy appearance is due to eruption of the lavas underwater.
14. Unconformity - an erosional surface between two units of rock. Whatever went on during that time… is unknown. The rocks are gone, weathered, and eroded into sediment to be transported for deposition somewhere. Could be close by, could be far, far away in another basin.

VITA

Tai was born and raised in El Paso, TX. She earned her Bachelor of Science in Geological Sciences at the University of Texas at El Paso in December of 2014. She enjoys rock climbing, aerial arts, and backpacking, even though backpacking is kind of like a busman's holiday for her. She has three delightful cats and is a really good cook.

Contact Information: tai.subia@gmail.com